CHAPTER 1

Transport of Ions, DNA Polymers, and Microtubules in the Nanofluidic Regime

DEREK STEIN[1,2], MARTIN VAN DEN HEUVEL[1], AND CEES DEKKER[1]

[1] Kavli Institute of Nanoscience, Delft University of Technology, Delft, The Netherlands

[2] Present address: Physics Department, Brown University, Providence, RI, USA

1.1 INTRODUCTION

Lab-on-a-chip fluidic technology takes inspiration from electronic integrated circuits, from which its name is derived. Lab-on-a-chip systems aim to improve chemical and biological analysis by using chip-based micromachining techniques to shrink the size of fluid handling systems.[1] In this way it borrows both the fabrication technology and the "smaller, cheaper, faster" paradigm from the integrated circuit industry. For silicon-based electronics, miniaturization eventually gave rise to qualitatively different transport phenomena because the device dimensions became comparable to important physical length scales, such as the de Broglie wavelength. Nanoelectronics has consequently become nearly synonymous with quantum mechanical effects. As fluidic devices are shrunk down to the nanoscale in the quest to manipulate and study samples as minute as a single molecule, it is natural to ask, "What physical phenomena should dominate in this new regime?"

As early as 1959, Richard Feynman recognized the challenges to controlling the motion of matter at the nanoscale in his famous speech, "There's plenty of room at the bottom".[2] He drew attention to the friction, surface tension, and thermal forces that would become important at such small dimensions. In the earliest nanofluidics experiments, the pioneering groups of Austin and Craighead observed unusual transport properties of DNA.[3-5] Channel dimensions comparable to the coil size of the polymers, called the radius of gyration, gave rise to strong entropic effects. Nanofluidics is in fact a regime where multiple physical length scales and phenomena become important, including the persistence length of a polymer, the Debye screening length for electrostatics, and the charge density along a channel surface.

In this chapter we review our studies of nanofluidic channels. These are the most fundamental structures in lab-on-a-chip devices, and represent the "wires" in the circuit analogy. It has therefore been natural to focus on the transport properties of nanofluidic channels, which we have investigated for small ions, DNA polymers that possess many internal degrees of freedom, and microtubules that undergo motion as part of their biological function. A recurring theme in our experiments has been the strong departure from bulk behaviour in sufficiently small channels. Different fluidic, statistical, or electrostatic effects can drive the crossover to a new regime in each case. This highlights

the importance of understanding multiple interacting phenomena as new nanofluidic applications are sought.

1.2 IONIC TRANSPORT

Ions are ubiquitous in aqueous solution, and manifestations of their motion have been the subject of inquiry for centuries. In recent years the transport of ions in nanoscale systems has attracted increasing attention because of its importance to fundamental biological processes, e.g. ion channels in cellular and sub-cellular membranes,[6] as well as man-made porous membranes for applications such as fuel cells,[7] and solid-state nanopores for single molecule DNA analysis.[8,9] The motion of ions is also coupled to the motion of the fluid by viscosity. This gives rise to electrokinetic effects such as electro-osmotic flow (EOF), which is widely applied in lab-on-a-chip technology.[10,11]

In order to study the transport of ions in the nanofluidic regime in detail, we fabricated channels with highly controlled geometries that were straightforward to analyze using theoretical calculations. A typical slit-like channel is illustrated in Figure 1.1. The 4 mm long, 50 μm wide channel was lithographically patterned between two 1.5 mm x 2 mm reservoirs on a fused silica substrate. A reactive ion plasma then etched the fused silica at a rate of 30 nm/min and was timed to stop when the desired channel height, h, had been reached. The channels were sealed by bonding them to a second, flat, fused silica substrate. Bonding was achieved using either a sodium silicate adhesive layer,[12] or by direct thermal bonding.[13] Pre-drilled holes allowed access to the reservoirs for introducing fluids or electrical connections.

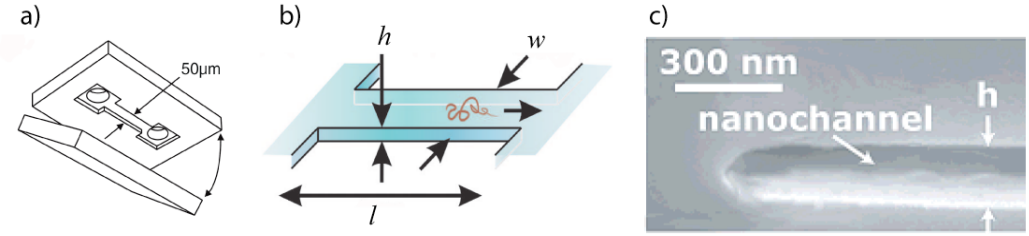

Figure 1.1 Slit-like nanochannels for transport measurements. (a) Nanofluidic channels are fabricated by bonding a flat, fused silica chip to a chip with a patterned channel structure and access holes. (image from ref.[14]) (b) The inner channel dimensions are well defined so that transport measurements of ions or polymers can be easily modeled theoretically. The channels are slit-like, with $l >> w >> h$. (image from ref.[15]) (c) A scanning electron micrograph of a channel cross-section. Adapted from reference [16] and reproduced with permission.

1.2.1 Electrically Driven Ion Transport

We have studied the electrically driven transport of ions in our nanofluidic channels.[17] The ionic current was measured while a DC voltage, ΔV, was applied across a channel filled with aqueous solution of a given potassium chloride (KCl) salt concentration, n. The salt dependence of the conductance is shown in Figure 1.2 for 5 channels ranging in height from h = 70 nm to h = 1050 nm. At high salt concentrations, the channel conductances scaled with the salt concentration and the channel height, just as would be expected for a bulk KCl solution. For low salt concentrations, however, the

conductance saturated at a minimum value independent of the channel height, and was orders of magnitude higher than would be expected from the bulk conductivity of the fluid.

The ionic conductance saturation results from the electrostatic influence of the charged channel walls on the ionic fluid. The silica surface is negative in solution at neutral pH, and therefore attracts positive counter-ions, while repelling negative co-ions. The thin region of fluid near the surface in which a net charge density is created is called the double layer.[18] It is the transport of mobile counter-ions in the double layer that accounts for the extra conductance observed at low salt concentrations.

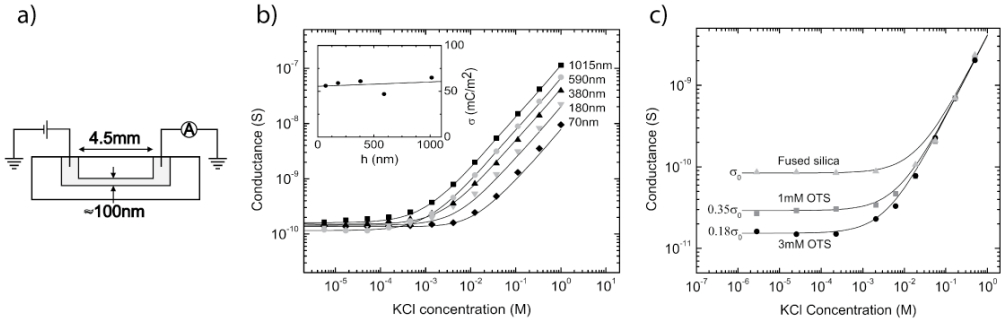

Figure 1.2 Surface-charge-governed ion transport in nanofluidic channels. (a) Cross-sectional illustration of a channel and the measurement apparatus configuration. (b) Salt concentration dependence of the DC ion conductance in a 50 μm wide channel. The solid lines are fits to the ion transport model described in the text. The values of σ obtained from the fits are plotted against h (inset). (c) The conductance of 87 nm high channels filled with 50% isopropanol, 50% KCl solution. The channels were treated with the indicated concentrations of OTS. Adapted from reference [17] and reproduced with permission.

The conductance of nanofluidic channels can be understood quantitatively. It is necessary to account for all the ions, including the double layer, and properly couple their motion to that of the fluid. We have modelled the electrostatic potential in the double layer using the nonlinear Poisson-Boltzmann (PB) equation, which is the conventional mean field theory that describes the competition between electrostatic and entropic forces on the ions:

$$\frac{d^2\psi(x)}{dx^2} = \kappa^2 \sinh(\psi(x)) \tag{1.1}$$

Here $k_B T\psi(x)/e$ is the electrostatic potential at height x from the channel mid-plane, e is the electron charge, $k_B T$ is the thermal energy, $1/\kappa$ is the Debye screening length, defined by $\kappa^2 = 2e^2 n/(\varepsilon\varepsilon_0 k_B T)$, and $\varepsilon\varepsilon_0$ is the permittivity of water. The Debye length sets the range of electrostatic interactions in solution. It is inversely related to salt concentration, increasing from $1/\kappa = 1$ nm at the roughly physiological salt concentration of $n = 100$ mM, to $1/\kappa = 10$ nm at $n = 1$ mM, and to $1/\kappa = 1$ μm in de-ionized water.

The exact solution for $\psi(x)$ in the slab geometry is known,[19] which allows us to calculate the exact (mean field) distribution of ions in our channels. The solution remains valid even when the double layers from opposing channel walls overlap. Moreover, the motion of ions is coupled to the fluid flow via the Stokes equation:

$$\eta\frac{d^2u(x)}{dx^2} - \frac{\Delta V}{l}\frac{\varepsilon\varepsilon_0 k_B T}{e}\frac{d^2\psi(x)}{dx^2} + \frac{\Delta p}{l} = 0 \tag{1.2}$$

where $u(x)$ is the fluid velocity, Δp is the pressure difference across the channel, and l is the length of the channel. We take $\psi(x)$ to be the equilibrium distribution, which is justified as long as the applied electric field gradients are too weak to significantly distort the double layer, i.e. smaller than $k_B T\kappa$.[20] It is also conventional to apply the no-slip boundary condition at the channel surfaces.

In the absence of an applied pressure gradient and taking the electrical mobility of the ions to be the bulk value, the solutions to Equations 1.1 and 1.2 can be used to calculate the total conductance of a channel. This was the approach used by Levine to calculate the ionic conductance in a narrow channel with charged walls.[21] However in order to accurately describe our experimental conductance data, it was necessary to replace the constant surface potential boundary condition that had been commonly used. We found that a constant effective surface charge density, σ, described the data extremely well and could be imposed on our transport model using Gauss' Law, i.e.

$$\sigma = \pm \frac{\varepsilon \varepsilon_0 k_B T}{e} \left. \frac{d\psi}{dx} \right|_{x=\pm h/2} \tag{1.3}$$

Our ionic transport model described the experimental data very well, as can be seen from the theoretical fits in Figure 1.2(b). The model contains only a single fit parameter, namely σ, which was found to agree well with published values for silica surfaces obtained by chemical titration experiments.[22]

The ion transport model also provides insight into the very different behaviour that was observed in the high and the low salt regimes. At high n, the number of ions in the double layer is overwhelmed by the number in the bulk fluid. The conductance of a nanochannel at high n therefore increases with n just as the conductivity of bulk solution. At low n, by contrast, the counter-ions in the double layer dominate. Their number is fixed by the requirement of overall charge neutrality, and so the conductance of the nanochannel becomes governed by the charge density at the surfaces. The crossover between high-salt and low-salt behaviour occurs when $|\sigma| \approx enh$ for monovalent salt. It is important to note that this does not correspond to double layer overlap. The data in Figure 1.2(b) clearly show, for example, that a 380 nm high channel is in the low-salt conductance plateau at $n = 10^{-4}$ M, where the Debye length is only 30 nm.

Solid-state nanopores and nanotubes are systems in which ion transport in the low salt regime is particularly relevant. Due to their small diameter (<10 nm typically), the onset of the conductance plateau in a nanopore occurs at salt concentrations as high as hundreds of millimolar. In addition, nanopore experiments typically involve the insertion of an individual DNA molecule, which is itself a highly charged object. The backbone of double-stranded DNA carries two electronic charges for every 3.4 Å of length. DNA insertion into a solid-state nanopore therefore entrains a high concentration of mobile counter-ions into the pore, which actually increases the measured conductance for salt concentrations below ~0.4 mM.[23-25]

The electrically driven transport of ions in nanochannels reveals an interesting parallel with integrated circuits. The dependence of channel conductance on the surface charge is analogous to the conductance modulations in a field effect transistor (FET) that can be induced by the charge on the gate. It is therefore possible to "gate" the conductance of a nanofluidic channel by chemically modifying its surface charge density, as we have shown in Figure 1.2(c). The conductance of an h = 87 nm channel in the low-salt regime was clearly reduced by treatments with octadecyltrichlorosilane (OTS), whose attachment to silica neutralizes the surface. Other groups have employed this phenomenon as a sensing

mechanism for biological agents[26] or reported how the surface charge density of a nanochannel can be voltage-modulated using gate electrodes to result in an "ionic transistor". [27,28]

1.2.2 Streaming Currents

Ions are displaced in a pressure-driven flow because of the viscous drag between them and the fluid. In bulk solution, equal densities of positive and negative ions leave the fluid neutral, so no net charge transport occurs. In the vicinity of a charged surface, however, the excess of counterions in the double layer is advected by the flow and carries an electrical current. These so-called streaming currents can become increasingly important in nanofluidic channels, whose surface to volume ratio is particularly high.

We have measured streaming currents in nanofluidic channels between h = 70 nm and h = 1147 nm.[14] The relationship between the streaming current, I_{str}, and Δp was found to be linear, so we characterized a channel by its streaming conductance, S_{str}, defined as the slope $I_{str}/\Delta p$. The salt concentration dependence of S_{str} for a typical h = 140 nm channel is presented in Figure 1.3 and shows an extended plateau at low n that drops to a small fraction of the plateau value as n is increased beyond ~1 mM.

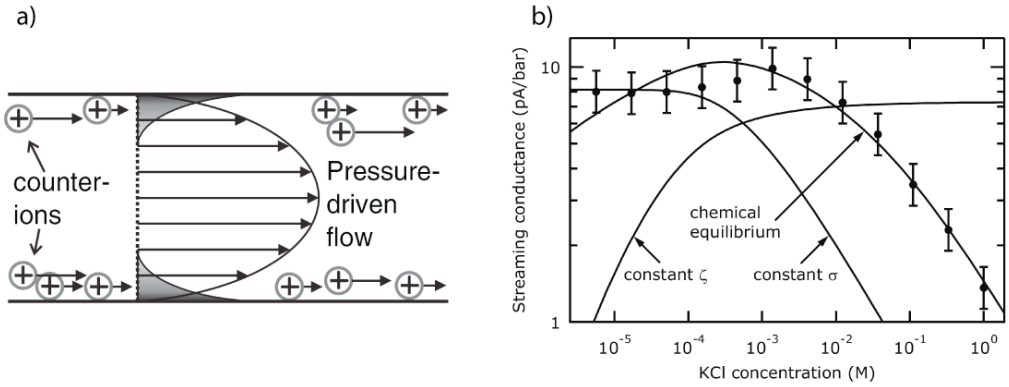

Figure 1.3 Streaming currents in nanochannels. (a) Schematic illustration of the origin of the streaming current. (b) Streaming conductance as a function of KCl concentration in a 140 nm high channel. The solid lines show model predictions for a constant surface charge, a constant surface potential, and a chemical equilibrium model discussed in the text. Adapted from reference [14] and reproduced with permission.

Streaming currents can be analyzed within the same theoretical framework as electrophoretic ion transport. The applied pressure, Δp, generates a parabolic (Poiseuille) fluid velocity profile that is maximal in the centre of the channel and stationary at the surfaces according to Equation 1.2. The distribution of ions that is described by the PB equation (Equation 1.1) is advected at the local fluid velocity. The streaming conductance is therefore highest at low n because the Debye length extends into the centre of the channel, where the fluid velocity is highest. We have found, however, that the constant σ boundary condition underestimates the streaming conductance at high n, predicting an earlier decay in S_{str} than observed. This can be resolved by accounting for the chemistry of the silica channel, whose surface charge density is taken to be salt and pH dependent using a model described by Behrens and Grier.[29] It predicts that as n increases, the double layer consists increasingly of potassium counter-ions rather than H^+. This shifts the chemical equilibrium towards a more negatively charged surface and explains the extended streaming current plateau that is observed in Figure 1.3(b).

At this point, we note the discrepancy between the boundary conditions that best describe pressure-driven and electrophoretic transport of ions in the same fluidic channels. This observation is not new. The Poisson-Boltzmann model can be used to interpret measurements of an object's charge by different techniques, including electrokinetic effects such as ionic conductance and streaming currents, as well as direct measurements of electrostatic forces on micron-scale surfaces using surface force apparatus[30] and atomic force microscopy (AFM) techniques.[31] It has been experimentally found that these techniques yield values for σ that can differ by a factor of 10 or more. These discrepancies highlight the fact that the Poisson-Boltzmann model does not accurately describe the microscopic structure of the double layer all the way down to the charged surface. As a result, it is necessary to speak of the "effective charge", which is a model-dependent parameter that characterizes a system's behaviour for a particular type of experiment. The double layer picture has been gradually refined to achieve more consistent predictions that account for the effects of non-specific adsorption (the so-called "Stern Layer"), ion correlations, and finite ion size.[32-34]

1.2.3 Streaming Currents as a Probe of Charge Inversion

Streaming currents are a sensitive probe of the surface charge and can be used to study the details of the solid-liquid interface.[35] The current derives from charge transport in the diffuse part of double layer only, because ions in the bulk fluid carry no net charge, and it is generally accepted that the tightly bound counter-ions in the Stern layer (also called the inner Helmholtz plane) remain immobile in a pressure-driven flow.[36-38] An important advantage of an electrokinetic probe of the surface charge over direct AFM force measurements is that streaming currents remain reliable even at high salt concentrations. We have used streaming currents in silica nanochannels to investigate the phenomenon of charge inversion (CI) by multivalent ions.

Ions play a fundamental role in screening electrostatic interactions in liquids. Multivalent ions (where the ion valency Z exceeds 1) can exhibit counterintuitive behaviour by not only reducing the effective charge of a surface, but by actually flipping its sign (Figure 1.4(a-b)). This phenomenon has been proposed to be relevant in important biological situations such as DNA condensation, viral packaging, and drug delivery.[39-41] CI, however, cannot be explained by conventional mean-field theories of screening such as the Poisson-Boltzmann model.

Shklovskii proposed an analytical model that assumes that multivalent counter-ions form a two-dimensional strongly correlated liquid (SCL) at charged surfaces and invert the surface charge above a critical concentration.[42] This effect is driven by the interaction parameter $\Gamma = \frac{\sqrt{\left|\sigma_b Z^3\right| e^3/\pi}}{4\varepsilon\varepsilon_0 k_B T}$ and is therefore strong for high Z and bare surface charge, σ_b. Besteman used AFM force measurements[43,44] to show that the SCL model accurately describes the dependence of c_0 on surface charge, dielectric constant, and ion valence for Z=3 and 4.

We first validated streaming current measurements as a new technique for studying CI by reproducing the findings for the Z=3 cation, cobalt(III)sepulchrate (CoSep), which is well understood both theoretically and experimentally. We then used streaming currents to test CI by divalent cations, for which earlier results had been inconclusive.[45-49] Figure 1.4(c) shows clear evidence for CI by the divalent cations Mg^{2+} and Ca^{2+} near the same high concentration of ~400 mM. This result is interesting for two reasons. First, these

divalent ions are relevant in biology. Second, this is an example of CI in a regime where the inter-ionic coupling is weak. The validity of the SCL model does not extend to Z=2, so these experiments provide a practical guide to theoretical refinements.

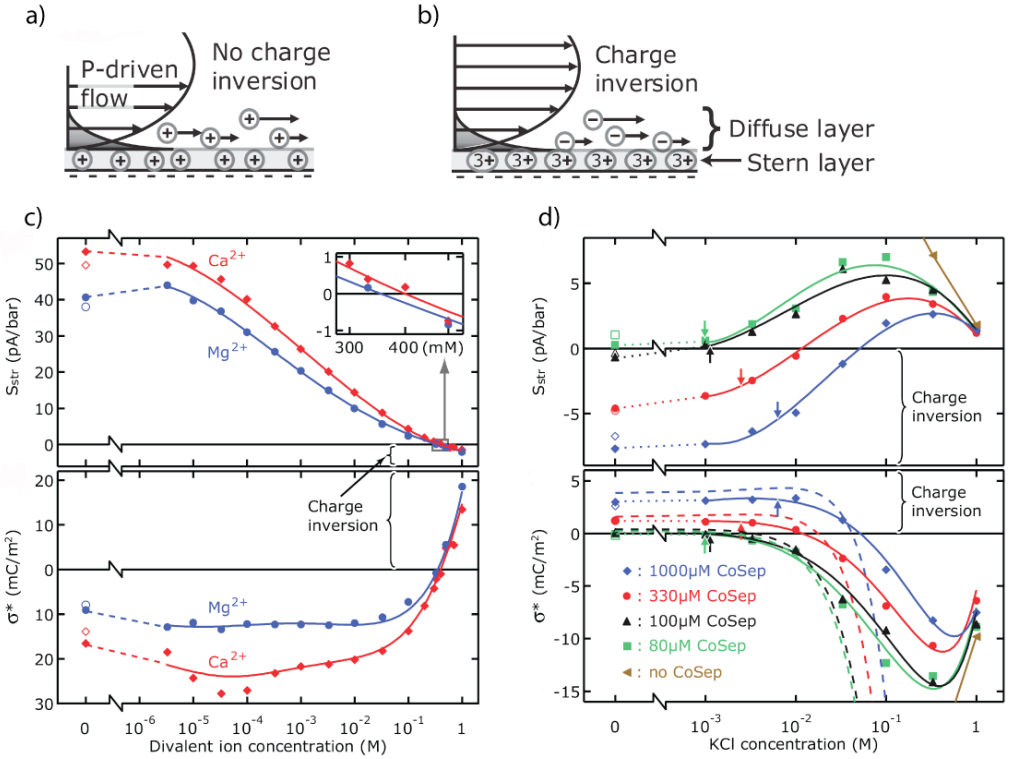

Figure 1.4 Studies of charge inversion using streaming currents. (a) Schematic illustration of the streaming current with screening by monovalent salt and (b) the effect of charge inversion by trivalent cations. (c) Divalent ion concentration dependence of (top) the streaming conductance and (bottom) the effective surface charge. The solid lines are guides to the eye; open symbols indicate measurements after each sweep from low to high concentration. The inset highlights the charge inversion concentration region. (d) The streaming conductance (top) and the effective surface charge (bottom) are plotted as a function of KCl concentration for various CoSep concentrations. The solid lines are guides to the eye; the dashed lines are model curves discussed elsewhere. Adapted from reference [35] and reproduced with permission.

The streaming current technique also allowed us to investigate the effects of monovalent salt on CI. High concentrations of monovalent salt (~150 mM) are typically present under physiological conditions in biological systems. This is expected to lead to screening of the surface charge and of multivalent ions. It was unclear, however, how this would affect CI. Our measurements showed that increasing concentrations of monovalent salt weaken and ultimately cancel CI by the trivalent cation CoSep (Figure 1.4(c)). The influence of monovalent salt on CI could be understood within a refined model of the SCL model up to the moderate concentrations at which CI was negated.

1.2.4 Electrokinetic Energy Conversion in Nanofluidic Channels

Electrokinetic phenomena exhibit a coupling between the transport of fluid and electricity. This presents interesting technological opportunities, such as for the electrical pumping of fluid by electro-osmosis, which has become important in microfluidics. In a reciprocal fashion, a pressure-driven fluid flow through a narrow channel carries a net

charge with it that induces both a current and a potential when the charge accumulates at the channel ends. These streaming currents and streaming potentials can drive an external load, and therefore represent a means of converting mechanical work into useful electrical power. The notion of employing electrokinetic effects in an energy conversion device is not new,[50] but has received renewed attention in the context of micro- and nanofluidic devices, whose geometries and material properties can be engineered to optimize performance.[16,51-54] High energy-conversion efficiency and high output power are the requirements for such a device to be practical. We have evaluated the prospects for electrokinetic energy conversion both theoretically[16] and experimentally.[54]

A fluidic device capable of electrokinetic energy conversion consists of an inlet and an outlet that are connected by one or more channels with charged walls (Figure 1.5). Its electrokinetic properties in the linear regime are defined by the response of the ionic current, I, and the volume flow rate, Q, to the application of an electrochemical potential difference, ΔV, or a pressure difference, Δp, between the inlet and the outlet according to:

$$I = \frac{dI}{d\Delta p}\Delta p + \frac{dI}{d\Delta V}\Delta V = S_{str}\Delta p + \frac{\Delta V}{R_{ch}} \tag{1.4}$$

$$Q = \frac{dQ}{d\Delta p}\Delta p + \frac{dQ}{d\Delta V}\Delta V = \frac{\Delta p}{Z_{ch}} + S_{str}\Delta V \tag{1.5}$$

where R_{ch} is the electrical resistance, Z_{ch} is the fluidic impedance, and S_{str} is the streaming conductance of the channel. Only three quantities are needed to fully describe the device because the voltage-driven fluid flow rate and the pressure-driven ionic current are related by the Onsager identity,[55] $dQ/d\Delta V = dI/d\Delta p \equiv S_{str}$ which expresses the reciprocity between electrically induced fluid flows and flow-induced electrical currents.

The energy conversion efficiency is defined as the electrical power consumed by the external load divided by the input mechanical pumping power and is found to have a maximum value of $\varepsilon_{\max} = \alpha/\left(\alpha + 2\left(\sqrt{1-\alpha}+1-\alpha\right)\right)$ at the optimized load resistance $R_L = R_{ch}/\sqrt{1-\alpha}$, where $\alpha = S_{str}^2 Z_{ch} R_{ch}$. The values of R_{ch}, Z_{ch}, and S_{str} for a particular device are determined by its geometry and the distribution of ions and fluid flows within it. We have used the theoretical framework outlined above to theoretically evaluate $\varepsilon_{\max}$ for slit-like channels.

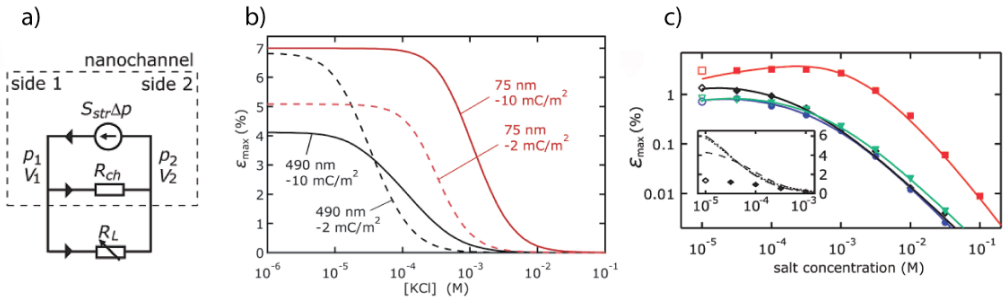

Figure 1.5 The efficiency of electrokinetic energy conversion in a nanofluidic channel. (a) Equivalent circuit of a nanochannel connected to a load resistor. (b) KCl concentration dependence of ε_{max} calculated using the model described in the text. The channel height and surface charge are as indicated. (c) Measured salt concentration dependence of ε_{max} for KCl, h = 75 nm (red); KCl, h = 490 nm (red); and KCl (blue) and LiCl (green) for the same h = 490 nm channel. Adapted from references [16, 54] and reproduced with permission.

The calculated n-dependence of ε_{max} shows that the highest energy conversion efficiency occurs in a low-*n* plateau, followed by a decay towards zero efficiency at high *n* (Figure 1.5(b)). The plateau region extends to higher *n* for smaller channels: up to $n = 10^{-5}$ M for a $h = 490$ nm channel and up to $n = 10^{-4}$ M for a $h = 75$ nm channel. This behaviour can be understood intuitively; in thin nanochannels and at sufficiently low salt concentrations, the double layers of opposing channel surfaces overlap, and electrostatic forces expel co-ions from the channel leaving only counter-ions. Because co-ions do not contribute to the electrical power generated by streaming currents, but instead provide an additional pathway for power dissipation through ionic conductance, they can only detract from the energy conversion efficiency. In addition, the extended double layers increase the concentration of counter-ions in the centre of the channel, where the fluid velocity is highest.

Our experiments confirmed that the maximum energy conversion efficiency occurs in the low salt regime. Figure 1.5(c) shows our experimental study of ε_{max} as a function of salt concentration for three channel heights. The energy conversion efficiency was found to be roughly constant at low *n*, and then decreased strongly at higher *n*. As predicted, the transition between the low and high salt regimes occurred at higher salt concentrations for smaller channels, for example, at $10^{-3.5}$ M for $h = 75$ nm versus $10^{-4.5}$ M for $h = 490$ nm.

We measured a peak energy conversion efficiency of ~3% for $h = 75$nm and KCl solution. This was less than half of the 7% efficiency that was predicted. We noted that this discrepancy could be reconciled by positing a finite conductance in the Stern layer, which is taken to be a layer of mobile counter-ions behind the no-slip plane on the channel. The counter-ions in the Stern layer consequently dissipate energy by electrical conductance without being advected by the pressure-driven flow. This model of the double layer was used to fit R_{ch}, S_{str}, and the efficiency data in Figure 1.5(c).

Clearly, a strategy is needed to significantly enhance efficiency if electrokinetic energy conversion is to be practical. An intriguing possibility that has recently been considered is to induce hydrodynamic slip at the surface of a channel.[56-58] A finite fluid velocity at the channel surface would increase the transport of counter-ions that concentrate there and eliminate the Stern layer by placing the extrapolated no-slip plane behind the channel surface. Recent experimental work and molecular dynamics simulations point to smooth and hydrophobic surfaces as conditions that promote slip.[59] The implication of a moderate degree of slip, characterized by a 30 nm slip length, is an energy conversion efficiency predicted to be 40%.[58] The extraordinarily long slip lengths recently reported for carbon nanotubes[60,61] imply very useful efficiencies exceeding 70%.

1.3 POLYMER TRANSPORT

Polymers are fundamental to biology. The genetic programs of all living systems are stored, translated, and executed at the molecular level by specialized polymers – DNA, RNA, and proteins, respectively.[62] These molecules contain valuable information regarding identity, biological function, and disease. This makes polymers important targets of lab-on-a-chip bioanalysis.

Length-separation is the most widespread analytical task for polymers, and is commonly accomplished by electrophoresis in a sieving medium such as a gel.[63,64] The interactions between polymers and the gel lead to length-dependent migration velocities.

Lab-on-a-chip devices were first reduced in size from the microscale to the nanoscale in a quest to control such interactions and create artificial separation devices. In nanofluidic channels small enough to restrict a polymer's internal degrees of freedom, it was found that entropic forces become important, giving rise to effects that have been exploited in novel separation strategies such as artificial gels[3] and entropic trap arrays.[65]

The transport of polymers within microfluidic and nanofluidic channels remains of central importance to lab-on-a-chip technology, but our understanding of the topic is far from complete. Polymers can be subjected to a wide variety of confining geometries, fluid flows, or electric fields. In this section we summarize our efforts to understand how polymers behave in situations that commonly arise in nanofluidics, such as parabolic fluid flows and electric fields.

1.3.1 Pressure-Driven Polymer Transport

It is straightforward to apply a pressure difference across a fluidic channel, and this has long been used to drive transport in chromatographic chemical separations. In contrast with electrical transport mechanisms such as electrophoresis or electro-osmotic flow, a pressure gradient generates a parabolic flow profile that leads to hydrodynamic dispersion, called Taylor dispersion, and flow speeds that depend strongly on the channel size.[10] These perceived disadvantages have made pressure-driven flows less popular than electrokinetic mechanisms in micro- and nanofluidic applications. The interaction of a parabolic flow with a confined flexible polymer had consequently remained unexplored.

We investigated the mobility and dispersion of long DNA polymers in a pressure-driven fluid flow in slit-like nanofluidic channels.[15] The centre-of-mass motion of individual molecules was tracked by epifluorescence optical microscopy and analyzed to determine the mobility and the dispersion of DNA. We investigated the influence of applied pressure, channel height and DNA length, L. Our results reveal how length-dependent and length-independent transport regimes arise from the statistical properties of polymer coils, and that the dispersion of polymers is suppressed by confinement.

1.3.1.1 Pressure-Driven DNA Mobility

Our experiments showed that the mean velocity of DNA, $\overline{V}$, increased linearly with Δp for a given L and h. To best reveal the dependence of pressure-driven DNA transport on L and h, we first defined a pressure-driven DNA mobility, ν, as the slope of $\overline{V}$ vs. Δp, i.e. $\overline{V} = \nu \Delta p$. We then plotted the ratio ν / ν_λ for each DNA length in the same channel, where ν_λ is the mobility of 48.5 kbp-long λ-DNA (Figure 1.6). This approach provided a measure of mobility that was insensitive to microscopic channel irregularities.

Two distinct regimes of pressure-driven transport can clearly be identified in Figure 1.6. In large channels (h > ~2 μm), the mobility of DNA increased with polymer length, with the mobility of λ-DNA exceeding that of 8.8 kbp-long DNA by 12% in h = 3.8 μm channels. In thin channels (h < ~1 μm), the mobility was found to be independent of length within experimental error. In order to explain the pressure-driven motion of DNA, we must consider the statistical distribution of DNA across a slit-like nanochannel. Thermal forces contort a DNA polymer into conformations that simultaneously sample different regions of the fluid flow. We assume that each segment of DNA moves at the local fluid velocity and take the centre-of-mass velocity to be the average over all segments, according to:

$$\overline{V} = \int_{-h/2}^{h/2} \rho(x)u(x)dx \Big/ \int_{-h/2}^{h/2} \rho(x)dx \tag{1.6}$$

where $\rho(x)$ is the average concentration of DNA segments across the channel. We can calculate $\rho(x)$ by modelling the polymer coil as a random flight whose equilibrium conformations are described by the Edwards diffusion equation[66]:

$$\frac{b^2}{6}\nabla^2 P(x,s) = b\frac{\partial P(x,s)}{\partial s} \tag{1.7}$$

where $P(x,s)$ is the probability that paths of contour length s end at height x, and b is the Kuhn length, which characterizes the stiffness of the polymer. From this probability distribution, the average density of polymer segments is given by,

$$\rho(x) = \int_0^L P(x,s)P(x,L-s)dx \tag{1.8}$$

The confinement of a polymer to a slit geometry was first treated by Casassa[67] and Casassa and Tagami[68] by imposing non-interacting boundary conditions at the walls, i.e. $P(\pm h/2) = 0$. We have used Casassa's exact result for $P(x)$ to calculate the mobility of DNA polymers in our channels. The values of b were fixed by matching the known radius of gyration for each polymer length, R_g, with the coil size of a random flight polymer according to $R_g = \sqrt{(Lb)/6}$. We note that this procedure implicitly includes polymer self-exclusion effects, which are not explicitly modelled by Equation 1.7.

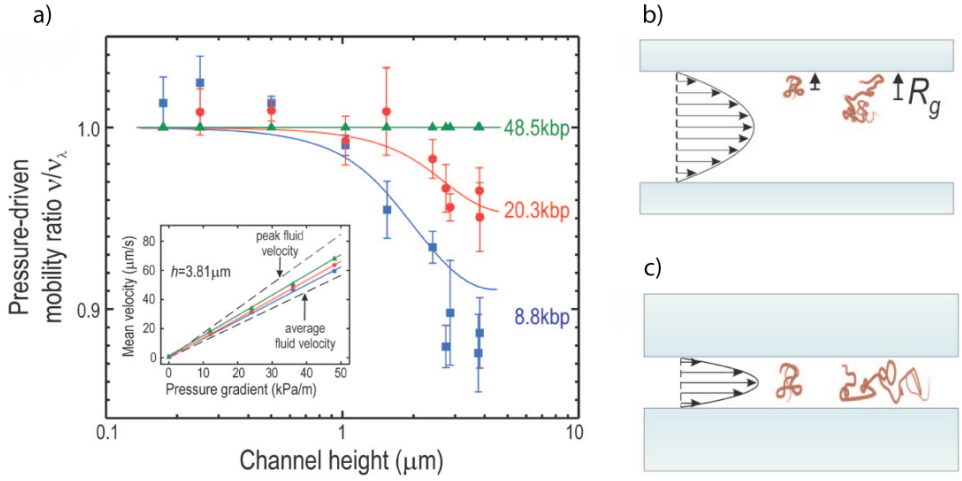

Figure 1.6 Pressure-driven DNA mobility in nanofluidic channels. (a) (inset) The average velocity of DNA molecules in an h = 2.73 μm channel versus applied pressure gradient. The slope of the curve defines the pressure-driven mobility, ν. (main panel) The ratios of ν for the indicated DNA fragment lengths to ν_λ for 48.5 kbp-long DNA. The solid lines indicate predictions of the polymer transport model described in the text. (b) Schematic DNA configurations in a wide channel, where the molecules' centre of mass is excluded from a region of length R_g from the channel wall. Long molecules are confined to the high velocity region of the flow, and consequently move faster than shorter molecules. (c) Schematic DNA configurations in a narrow channel, where DNA mobility is independent of length. Adapted from reference [15] and reproduced with permission.

The results of our polymer transport model are plotted together with the mobility data in Figure 1.6. The model clearly predicts both length-dependent and length-independent regimes, as well as the crossover between them for all DNA lengths. The quantitative agreement between our model and the data is also good. The model only mildly overestimates the mobility of the shortest DNA fragment in the largest channels. We note that our model contains no fitting parameters. Its only inputs are the known lengths and radii of gyration of the DNA fragments.

The physical picture behind the two pressure-driven transport regimes can be understood as follows: In channels that are large compared with the polymer coil size, molecules can diffuse freely in the central region of the channel. However, they are impeded from approaching the walls closer than the radius of gyration. Long DNA molecules are therefore more strongly confined to the centre of the channel, where the fluid velocity is highest. This explains why long molecules travel faster in large channels and corresponds to the concept of "hydrodynamic chromatography" of polymers.[69] In channels that are small compared with the polymer coil size, the DNA is squeezed into new conformations. Although the shapes of longer molecules may be more extended in the plane of the channel, the concentration profile of DNA segments across the channel height is length-independent. This explains why the mobilities of long and short DNA molecules are the same in the thin channel regime.

1.3.1.2 Dispersion of DNA Polymers in a Pressure-Driven Flow

The dispersion of DNA arises from the fluctuations in a molecule's velocity. We have used the same pressure-driven DNA measurements to study this fundamental transport property. We quantified velocity fluctuations by the dispersion coefficient, D^*, defined by $2D^*\Delta t = \left\langle (\Delta z - \overline{V}\Delta t)^2 \right\rangle$. Here $\left\langle (\Delta z - \overline{V}\Delta t)^2 \right\rangle$ is the mean square displacement of a molecule from its original position along the channel length, translated with the mean velocity in the time interval Δt.

Dispersion in a pressure-driven flow is understood to originate from two distinct mechanisms. First, the random thermal forces exerted on a particle by the surrounding fluid give rise to Brownian motion, which we parameterize by the thermal self-diffusion coefficient, D_0. Second, hydrodynamic dispersion also arises in a non-uniform flow. A particle in a fast moving region of the flow is pulled ahead of a particle near the wall, where the flow is slow. Taylor first considered the interplay between these thermal and hydrodynamic dispersion mechanisms for point particles, and so the phenomenon is known as Taylor dispersion.[70]

Generalized Taylor dispersion theory[71] predicts that D^* can be expressed as the sum of a purely thermal term and a convective term proportional to $\overline{V}^2$:

$$D^* = D_0 + \alpha_T \overline{V}^2 \tag{1.9}$$

Here, we have introduced a parameter, α_T, to quantify the hydrodynamic component of dispersion. We have found that Equation 1.9 fits our experimental data extremely well, as shown in Figure 1.7(a) for two different channel heights. We have used such fits to extract experimental values for α_T.

The thermal self-diffusion of DNA was studied by considering dispersion in the absence of an applied pressure (where $\overline{V} = \alpha_T = 0$). We found that D_0 was suppressed with increasing confinement in thin channels, in good agreement with a famous scaling

relationship predicted by de Gennes.[72] This confirmed previous observations of the phenomenon[73-75] and extended its verified range to higher degrees of confinement. More recent measurements by the Doyle group have found subtle departures from the de Gennes predictions.[76]

To date, the hydrodynamic dispersion of long polymers has not been realistically modelled, so an appropriate prediction of α_T is not available. We instead compared the experimentally determined values of α_T to models of point-particle[77] and free-draining rigid sphere dispersion[69] as shown in Figure 1.7(b). Both models clearly fail to describe the observed behaviour. Taking DNA to be a point particle overestimates its dispersivity by more than an order of magnitude, whereas the rigid sphere model predicts a rapid drop to zero dispersion that was not observed.

These results suggest that Taylor dispersion theory needs to be extended in order to account for the unusual behaviour of polymers under confinement. Our experiments have nonetheless demonstrated empirically that the hydrodynamic dispersion of DNA polymers is greatly suppressed in nanochannels, which may be of benefit to analysis applications.

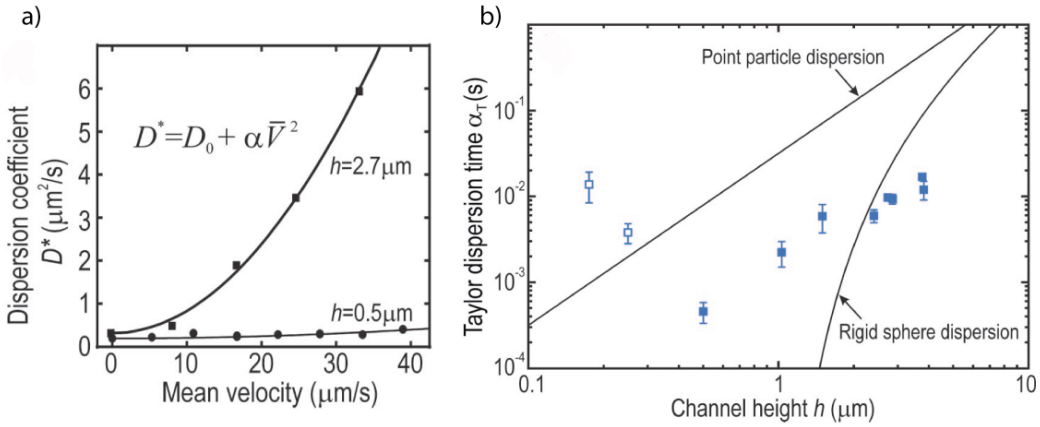

Figure 1.7 Taylor dispersion of DNA polymers in micro- and nanofluidic channels. (a) The dispersion coefficient of λ-DNA is plotted against its mean velocity for h = 2.73 and h = 500 nm. Solid lines indicate fits of $D^*=D_o+\alpha_T V^2$. (b) The height dependence of the measured values of α_T for 8.8 kbp-long DNA is compared with point-like and free-draining rigid particle models of Taylor dispersion.

1.3.2 Electrokinetic DNA Concentration in Nanofluidic Channels

For a chemical separation technique to be successful, an ensemble of sample molecules must first be collected in a narrow band from which they are typically "launched" into the separation region. The controlled concentration of analyte has therefore become an important goal of recent lab-on-a-chip research. Leading strategies include the use of nanofluidic filters,[78] micellar electrophoretic sweeping,[79] field-amplified sample stacking,[80] isotachophoresis,[81] electrokinetic trapping[82] and membrane pre-concentration.[83,84] We have recently discovered that in the nanofluidic regime, it is possible to take advantage of the unique transport properties of long polymers to concentrate them in an elegant way.[85] Our idea for DNA concentration was inspired by observations of surprising electrically driven DNA flow patterns in our slit-like nanochannels. Under a constant applied potential, DNA molecules aggregated near the end of the channel at the negative pole. At the same time, DNA was depleted from the opposite end of the channel. These dynamics were surprising because the axial velocity of DNA actually flips sign

twice along the length of the channel, and also because this behaviour was only observed at low (<mM) salt concentrations. At high salt concentrations (~60 mM), DNA migrated continuously from one pole to the other.

We sought to understand the origin of these dramatic DNA flows at low *n* so that we might induce the controlled pre-concentration of DNA at arbitrary salt concentrations. A polymer transport model similar to the one outlined in Section 1.3.1.1 explained our observations. In the case of electrically driven transport, we considered two driving terms. First, electrophoresis moves DNA relative to the fluid with a migration velocity, $\vec{v}_{elec}$, that is proportional to the local electric field. Second, the fluid itself is driven by electric fields because counter-ions in the double layer drag the fluid by electro-osmosis. The fluid flow then carries the DNA by advection with a velocity $\vec{v}_{advect}$.

A highly symmetric situation that is commonly found in micro- and nanofluidics is a constant electric field in a uniform channel. In this case $\vec{v}_{elec}$ and $\vec{v}_{advect}$ are both constant and proportional to each other. In general, however, the electric field can vary along the length of the channel, as can the electrophoretic force at the channel walls, e.g. due to conductivity and surface charge density variations, respectively. This establishes a competition between electrophoresis and advection that is well illustrated by the following example (Figure 1.8).

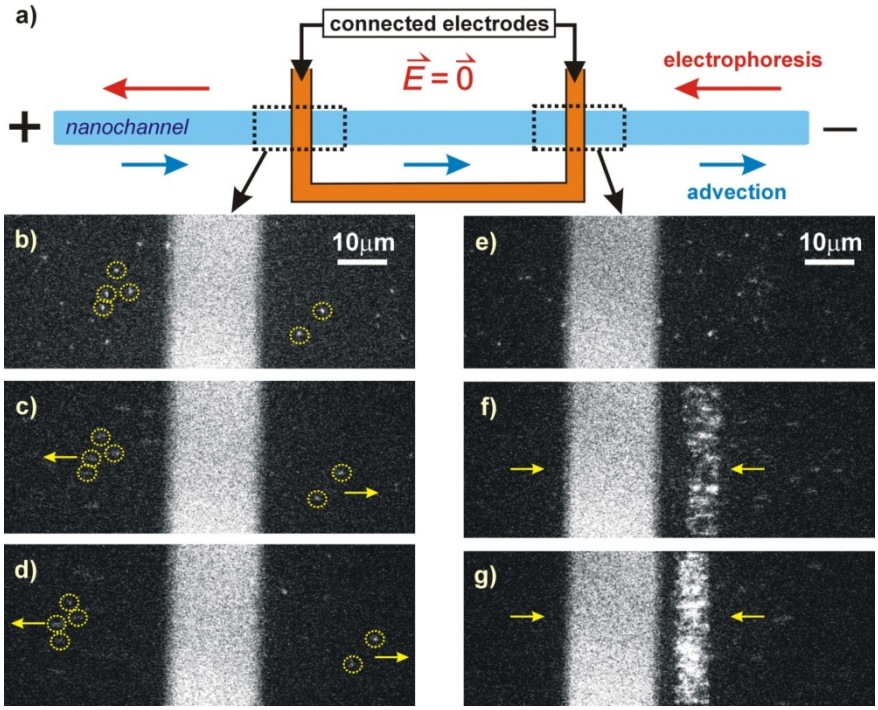

Figure 1.8 Inducing controlled DNA concentration and depletion in a 500 nm high nanofluidic channel. (a) Schematic top view of the device, showing the fluidic nanochannel intersected at two points by the connected electrodes. The electrodes do not block the channel but contact the fluid in order to cancel the electric field between them. The red and blue arrows indicate the predicted $\vec{v}_{elec}$ and $\vec{v}_{advect}$ in the different channel regions, respectively. Fluorescence micrographs show DNA molecules near the electrode towards the positive pole prior (b) to the application of 10V across the channel and then at increasing times after (c and d). The same molecules are circled in each image to highlight their motion away from the electrode. Near the electrode towards the negative pole, DNA molecules are shown prior to (e) the application of 10V and then after (f)–(g). Adapted from reference [85] and reproduced with permission.

We designed a nanofluidic device to concentrate DNA at a specified location, and at technologically relevant salt concentrations. The layout consisted of a slit-like channel intersecting an annular gold electrode at two points. The electrode was fabricated so as to contact the fluid in the channel, and maintain a constant electrochemical potential between the two intersection points. The electrode was embedded into the bottom surface so as to maintain the channel cross-section, and avoid impeding the fluid flow.

When a constant ΔV was applied across the channel, strong electric fields were generated near the ends, so $\vec{v}_{elec}$ dominated $\vec{v}_{advect}$ there, and DNA was pulled towards the positive pole. In the region between the electrodes, $\vec{v}_{elec}$ was suppressed. $\vec{v}_{advect}$, on the other hand, continued to push DNA towards the positive pole in the central region because the fluid is effectively incompressible and travels towards the negative pole at a constant flow rate Q. The net effect of these driving forces was to concentrate DNA at the electrode near the negative pole and deplete it from the other electrode. We note here that the details of the induced fluid flow are in fact complicated, involving re-circulating motion that would disperse point particles distributed across the channel height. It is the ability of a confined polymer to sample the entire flow profile that leads to an averaged value for $\vec{v}_{advect}$ and the possibility to electrically concentrate DNA. This nanofluidic pre-concentration method for polymers is appealing because it is entirely electrically driven. It is therefore straightforward to implement and control, and the integrated electrodes can also be used for other functions, such as driving the molecules into a separation device.

1.3.3 DNA Conformations and Dynamics in Slit-Like Nanochannels

In studying the transport of DNA polymers in nanofluidic channels, we have mainly focused on how polymers interact with imposed electric fields and fluid flows. The specific conformations that a molecule adopts, and their characteristic fluctuation rate, play important roles as the molecule interacts with its environment, e.g. the features of a separation device. We have recently sought to better understand the static and dynamic properties of DNA in confined environments, which is important for the design of single-molecule analysis and manipulation devices, and may provide insight into natural processes like DNA packaging in viruses[86] and DNA segregation in bacteria.[87] Here we outline some of our recent results on DNA conformations and dynamics in slit-like channels.[88]

We studied the conformations of DNA polymers under increasing degrees of confinement from their two-dimensional projections (Figure 1.9(a)). We analyzed fluorescent DNA images to compute the radius of gyration tensor for each conformation. The principal axes of these conformations were calculated from the eigenvalues of the radius of gyration tensor and used to quantify properties such as the coil size and molecular anisotropy. The measured distributions of the major and minor axis lengths are shown in Figure 1.9(b) (along with theoretical fits based on a statistical model that is presented elsewhere[88]). The dependence of the measured anisotropy on confinement was found to be consistent with the theoretical model by van Vliet and ten Brinke,[89] i.e. for decreasing h, the anisotropy first decreased due to an alignment of the longest molecular axis with the channel by rotation. Anisotropy then increased as confinement caused excluded volume interactions to stretch the molecule laterally.

Our experiments also found that the polymer coil size went through three distinct regimes with increasing confinement. The DNA was first compressed slightly in a manner consistent with predictions of van Vliet *et al.*[89] It then extended with confinement as predicted by the well-known scaling theory by de Gennes.[72] In the thinnest channels,

whose height was comparable to the DNA persistence length, the DNA size reached a plateau. This last regime is often referred to as the "Odijk" regime.[90,91] The characteristic relaxation time of the molecule, given by the autocorrelation of its size fluctuations, also revealed the same three regimes. The relaxation time decreased slightly with *h* in the highest channels, followed by a rapid rise in the de Gennes regime, and then a rapid decline in the Odijk regime. These observations of DNA in slits are consistent with previous observations of de Gennes and Odijk scaling in square channels. We note that the Odijk regime is somewhat different in the case of wide slits, because the polymer can bend back on itself without having to pay a large energetic price.

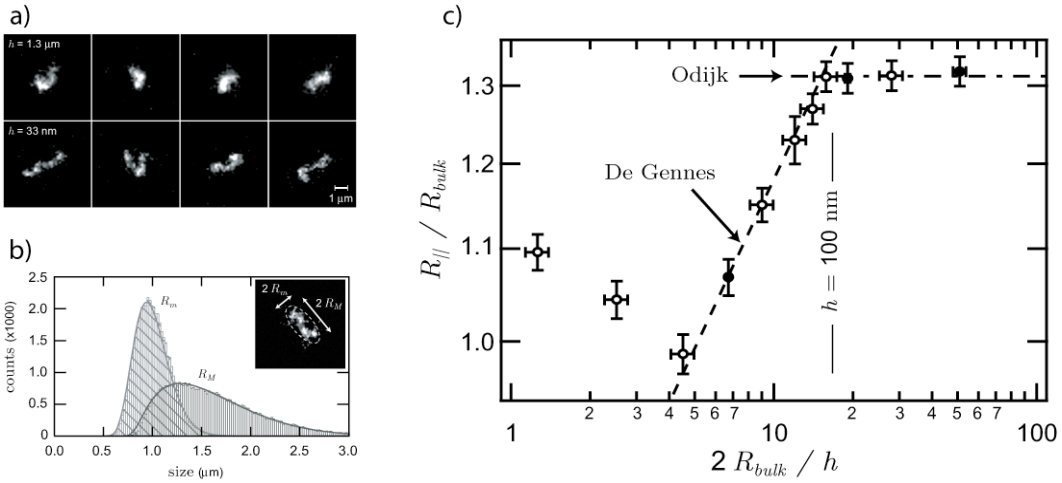

Figure 1.9 DNA conformations in nanofluidic slits. (a) Typical images of λ-DNA in 1.3 μm and 33 nm high channels. (b) Histograms of the major (R_M) and minor (R_m) axis lengths of λ-DNA for h = 107 nm. (inset) An image of a molecule indicating the calculated R_M and R_m. (c) The projection of the radius of gyration as viewed from above the slit versus confinement. The dashed line indicates the de Gennes scaling relationship. The dash-dotted line indicates the Odijk regime. Adapted from reference [88] and reproduced with permission.

1.4 MICROTUBULE TRANSPORT IN NANOFLUIDIC CHANNELS DRIVEN BY ELECTRIC FIELDS AND BY KINESIN BIOMOLECULAR MOTORS

When Richard Feynman contemplated the challenges associated with manipulating matter at the nanoscale back in 1959,[92] he could turn to biology for inspiration on how to cope with these issues. The biological cell contains the ultimate in nanomachines, with processes such as cell motility, energy production, protein assembly, cell division and DNA replication all originating from the activities of small protein machines.[93,94] Examples include the rotary motor that drives the bacterial flagella,[95] and the linearly moving motors, for instance, myosin that drives muscle contraction, or kinesin and dynein motors that drive the intracellular transport of materials.[96]

Biomotors are enzymes that contain moving parts and use a source of free energy to direct their mechanical motion. The linear-motion motors (kinesin, myosin, dynein) use the energy of the hydrolysis of adenosine-triphosphate (ATP), the cell's energy molecule, to move in discrete steps along tracks made of long protein polymers (actin filaments for myosin, microtubules for kinesin and dynein) that form the cytoskeleton that extends

throughout the cell.[97] The structural polarity of these filaments (denoted by a plus and minus end) allows unidirectional movement of the motors along their tracks. For example, a single kinesin consists of two motor domains that can step in discrete 8.2 nm steps (corresponding to the periodicity of a microtubule's protofilament) toward the plus end along a microtubule.[98] Upon each 8.2 nm step, kinesin can withstand an opposing force of up to 6 pN,[98,99] thus performing work of approximately 50 pN·nm. Since there is a tight coupling between a single step and the hydrolysis of a single molecule of ATP[100-102] (liberating ~80 pN·nm of free energy at cellular conditions), kinesins can work at an impressive ~60% efficiency.

One particularly active field of research is the use of biomotors for actuation and transport of materials in artificial nanofabricated environments.[103] In the first part of this chapter we describe recent advances in the exploitation of kinesin motors for nanotechnology. In particular we discuss the use of electric forces to manipulate the direction of individual microtubules at junctions. Thereafter, we describe the use of nanofabricated structures and electric fields for biophysical studies on single microtubules.

1.4.1 Electrical Manipulation of Kinesin-Driven Microtubule Transport

A molecular motor such as kinesin can potentially be used as the workhorse in miniaturized analytical systems or nano-electromechanical systems.[103-105] For example, active transport by molecular motors could be used for purification of materials against a flow, for the concentration of molecules, or for transport in increasingly smaller capillaries. These motors can be employed in either one of two geometries (Figure 1.10(a) and (b)). In the so-called bead assay (Figure 1.10(a)), mimicking the biological situation, a motor-coated cargo is transported along cytoskeletal filaments that are adsorbed onto a substrate. In the alternative geometry (Figure 1.10(b)), which is mostly employed, cytoskeletal filaments are propelled by surface-bound motors. In this gliding-assay geometry, the microtubules act as nanoscale trucks while transporting an attached cargo.

A considerable current effort in the field of molecular motor-assisted technology is aimed at building a nanoscale transport system in which biomotors are used for the active concentration of analyte molecules that are present in otherwise undetectably low quantities.[106-108] A schematic of such an envisioned device is pictured in Figure 1.10(c). Microtubule transporters, functionalized with antibodies specific to the analyte molecule of interest, bind molecules from a sample and transport them toward a second region on a chip, thereby concentrating the analyte and facilitating detection. En route, sensing and sorting capabilities are necessary.

An important step toward this goal has been the integration of kinesin motor proteins inside microfluidic channels.[109] The use of enclosed channels offers a great advantage for the confinement of motility to predetermined pathways. In the open trench-like structures that were used previously,[110-115] a common problem was that the motor-propelled microtubules collided with the sidewalls of the structures and were pushed out of their tracks. Another advantage of enclosed channels is that strong electric fields can be locally employed to manipulate individual (negatively charged) microtubules, as opposed to the large-scale effects of electric fields applied in open structures as previously demonstrated.[116-118]

We first show that microtubule motility can be reconstituted inside enclosed fluidic channels. To demonstrate this, we have fabricated micron-sized microfluidic channels in glass substrates (Figure 1.11(a)). We use e-beam lithography and wet-etching

to fabricate a network of open channels in fused-silica substrates. The width of the channels varies from several to tens of micrometers, and the depth of the channels is typically one micrometer or less. The channel structures were sealed with a second glass substrate (Figure 1.11(a) and (b)). The insides of the channels were coated with casein and kinesin motor proteins by flushing the protein-containing solutions through the channels. Then, upon adding a solution containing microtubules and ATP, microtubules bind to the surface-adsorbed kinesins and are subsequently propelled through the channels. The movement of microtubules is imaged by fluorescence microscopy (Figure 1.11(c)).

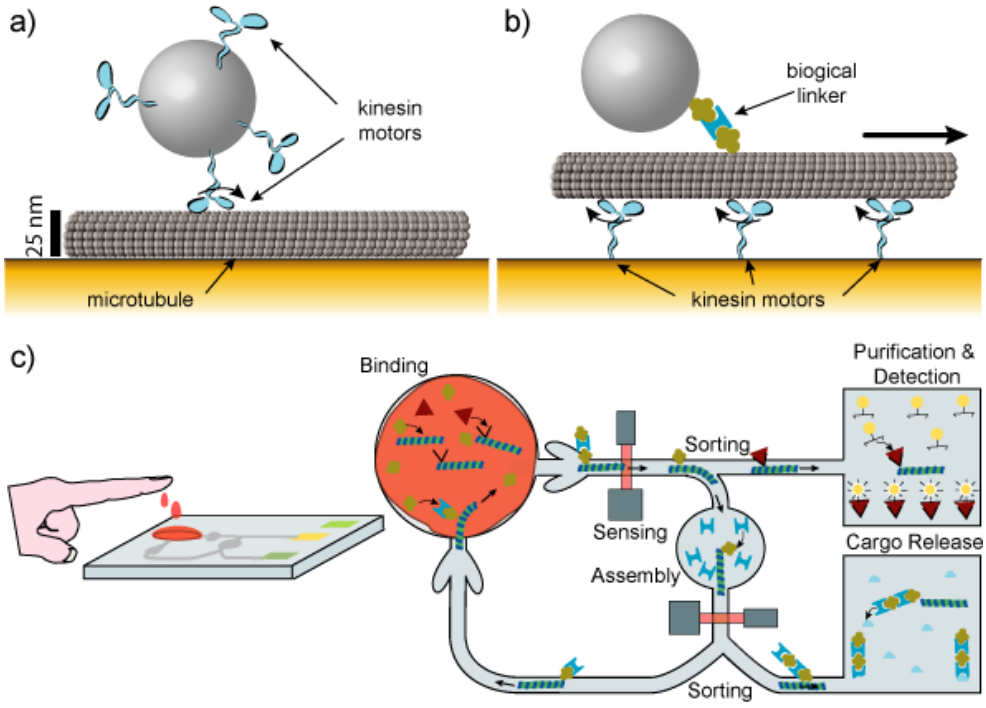

Figure1.10 Kinesin motors as transporters in artificial environments. (a) In the bead assay, motor-coated cargo moves along surface adsorbed cytoskeletal filaments. (b) In a gliding assay, surface-bound motors propel cytoskeletal filaments that can act as shuttles for a bound cargo. (c) Fictitious device combining diverse functionalities such as rectification and sorting of motility, purification and detection of analyte molecules, and the assembly and release of cargo molecules. Adapted from reference [103] and reproduced with permission.

We show that individual microtubules can be steered through application of electric fields. Steering of microtubules is a necessary prerequisite for imagined applications such as those depicted in Figure 1.10(c). To demonstrate this, we fabricated a Y-junction of channels across and through which a perpendicular channel was fabricated (Figure 1.11(d)). An electric field can be induced and confined inside this perpendicular channel through the application of a voltage difference between electrodes at either end of the channel. In Figure 1.11(d) we show a microtubule approaching a Y-junction, initially headed toward the left leg of the junction (t = 0 s). Upon application of an electric field in the perpendicular channel, an electric-field induced force acts in the opposite direction, gradually changing the course of the microtubule. Eventually it is steered into the right leg of the Y-junction (Figure 1.11(d), t = 20 s).

To illustrate the feasibility of a sorting application such as that depicted in Figure 1.10(c), we have employed electric forces to sort a population of microtubules carrying different cargos into different reservoirs on a chip (Figure 1.12). To this end we prepared and mixed microtubules that carry different colours (red and green) of fluorescent

molecules. Using a colour-sensitive camera to discriminate between the microtubules, red microtubules approaching a Y-junction were actively steered into the left leg of the junction, whereas green microtubules were sent in the opposite direction, simply by reversing the polarity of the electric field (Figure 1.12(a)). After a large number of such successful single-microtubule redirections one reservoir contained predominantly red microtubules (91 %) and the other reservoir contained predominantly green microtubules (94 %) (Figure 1.12(b)).[109]

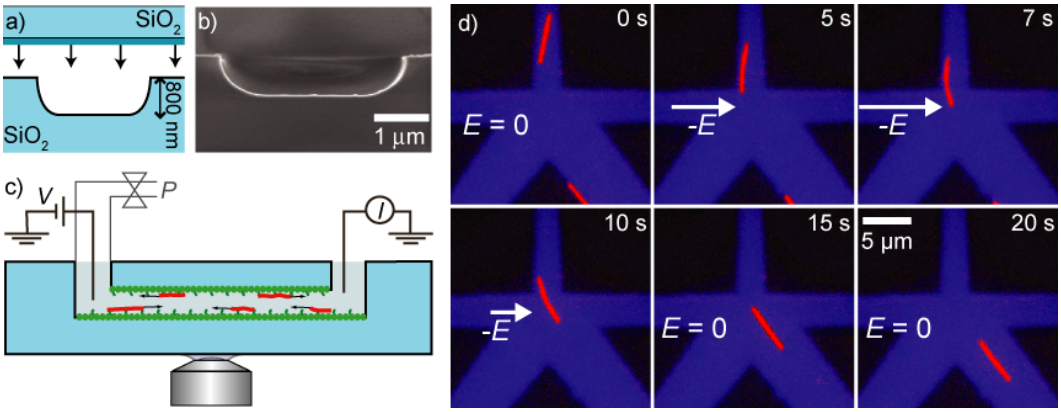

Figure 1.11 Electric forces can be used to steer individual microtubules in microfluidic channels. (a) Channels are fabricated in glass channels and sealed with a glass cover slip. (b) Scanning electron-microscopy image of a cross section of a channel. (c) Channels are coated with kinesin motor proteins and microtubules can be imaged moving through the channels by fluorescence microscopy. (d) A microtubule that approaches a Y junction from the top is steered through the use of electric forces into the right leg. The electric force points in the direction indicated, and the strength of the electric field is varied between 0 and 50 kV/m (indicated by length of arrow). Adapted from reference [109] and reproduced with permission.

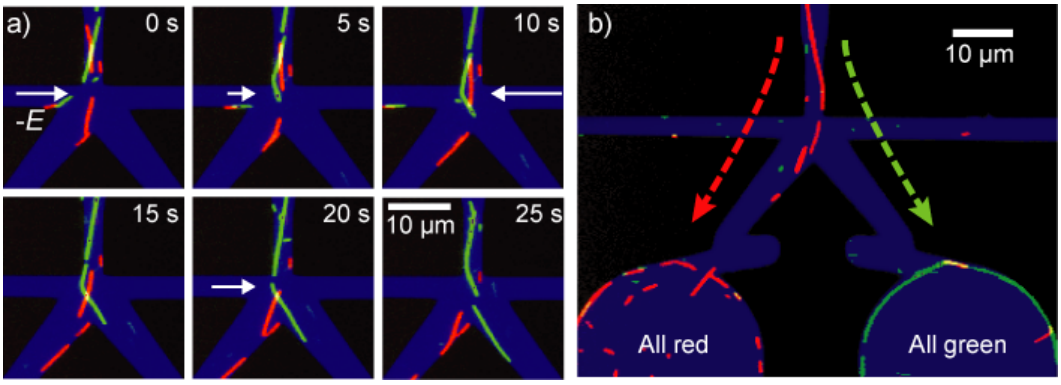

Figure1.12 On-chip sorting of a population of red and green-labeled microtubules. (a) By manually changing the polarity of the applied voltage, first a green microtubule is steered into the right leg of the junction (t = 0 and 5 s), then a red microtubule is steered into the left leg (t = 10 s), and finally a green microtubule is steered into the right leg again (t = 20 s). (b) The two legs of the junction lead to different reservoirs. After time, the right reservoir contains predominantly green microtubules, whereas the left reservoir contains red microtubules. Adapted from reference [109] and reproduced with permission.

In conclusion, the use of biomotors for sorting and transport of materials is an exciting development and could provide an interesting alternative to pressure-driven or electro-osmotic flow driven transport on a chip. However, the latter technologies are fairly well-developed, whereas many biomotor-powered applications are currently merely proof-of-principle demonstrations. At the moment, many speculative proposals for biomotor-driven applications still fail to be competitive when critically scrutinized and weighted against existing alternatives. Nevertheless, it may be that the application of biomotors for technology is currently only limited by the imagination and creativity of researchers and new opportunities may be found in yet unforeseen directions. Yet, the small size, force-exerting capabilities and possibilities for specific engineering of biomotors, for which currently no real alternatives exist, offers exciting opportunities that call for exploration.

1.4.2 Mechanical Properties of Microtubules Measured from Electric Field-Induced Bending

An interesting spin-off of the above mentioned experiments has resulted from the study of the mechanism that underlies the steering of individual microtubules. The curvature of microtubule trajectories under a perpendicular force of known magnitude is an amplification of the microscopic bending of their leading microtubule ends and thus provides an elegant measure of their stiffness. The stiffness of short microtubule ends, which are only sub-micrometer in our experiments, is of interest since recent experiments have indicated that the mechanical properties of microtubules on short length-scales can deviate considerably from their long-length behaviour.[119] Here, we describe experiments in which the observation of microtubule-trajectory curvatures under controlled perpendicular electric forces allows us to obtain an estimate of the mechanical properties of very short microtubule ends.[120] The use of nanofabricated structures for these experiments is beneficial, since it allows for a controlled and directed application of electric forces. Moreover, the high surface-to-volume ratio of microfluidic channels limits Joule-heating of the solution while an electric field is applied.

In order to study microtubule trajectories under perpendicular electric fields we fabricated channels in a perpendicular layout (Figure 1.13(a)). Microtubules enter the wide horizontal channel, in which a homogeneous electric field is present and, similarly to the steering experiments shown in Figure 1.11, their direction of motion is changed. In Figure 1.13(a) we show trajectories of microtubules that enter the electric field and gradually change their trajectory, in such a way to become aligned parallel and opposite to the electric field.

The mechanism of redirection is as follows (Figure 1.13(b)). The electric field induces a constant force density on the homogeneously charged microtubule in the direction opposite to the electric field. Kinesin molecules, distributed along the length of the microtubule, exert the opposing forces. This prevents movement of the microtubule perpendicular to its axis, which is confirmed by the data shown in Figure 1.13(b), where we show exactly overlapping traces of the leading and trailing-end coordinates of a microtubule moving in an electric field. Thus, the thermally fluctuating leading tip of the microtubule is biased into the direction of the applied force, thereby orienting the microtubule in a step-by-step fashion into the direction of the electric field.

The average curvature of the microtubule trajectory $\langle d\theta/ds \rangle$ (where the trajectory is described with coordinates θ and s (Figure 1.13(b)) relates to the perpendicular component of the applied field-induced force $f_{\perp}$ through the persistence length p and the average length $\langle d \rangle$ of the leading microtubule end as[120]

$$\left\langle \frac{d\theta}{ds} \right\rangle = \frac{\langle d \rangle^2}{3k_b Tp} f_\perp \tag{1.10}$$

Equation 1.10 allows us to determine the value of the tip persistence length from observations of the curvature of microtubule trajectories under a known force provided that the average tip-length is known. The magnitude of the field-induced force $f_\perp$ is proportional to the electric field E that we apply,[120,121]

$$f_\perp = \mu_\perp c_\perp E \sin\theta \tag{1.11}$$

Here, $\mu_\perp$ is the mobility of a microtubule for motion perpendicular to its axis during free electrophoresis and $c_\perp$ is the perpendicular hydrodynamic drag coefficient per unit length of a microtubule close to a surface. The value of $\mu_\perp$ can be measured through electrophoresis experiments on individual microtubules,[122] as we show in the final section of this chapter, and amounts to $\mu_\perp = -(1.03 \pm 0.01)10^{-8}$ m^2/Vs for these experiments. The value of the perpendicular hydrodynamic drag coefficient of a microtubule was measured by Hunt *et al.* as $c_\perp = (1.19 \pm 0.11)10^{-2}$ Ns/m^2.[123]

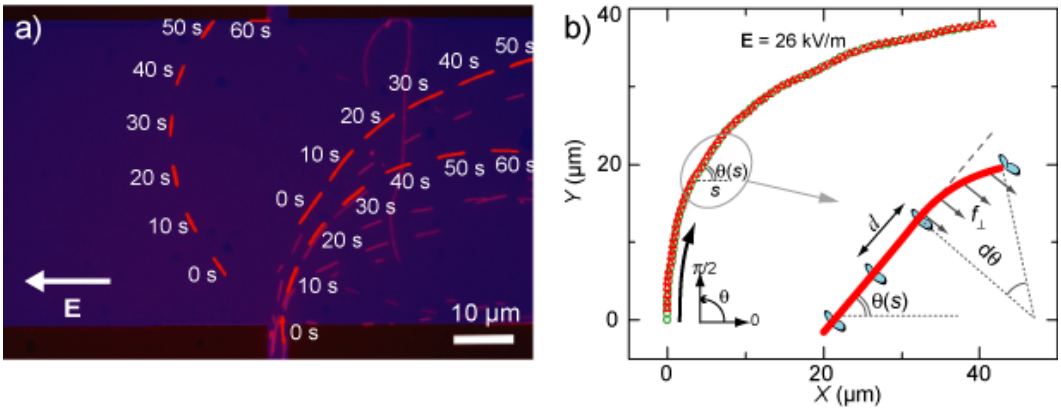

Figure1.13 The curvature of microtubule trajectories under an applied electric field. (a) Overlay of fluorescence images (with 10 s intervals) of microtubules moving under an electric field E = 26 kV/m. The microtubules enter from the small channel below and gradually become aligned with the electric field. (b) Overlapping coordinates of the leading (red triangles) and trailing (green circles) ends of a microtubule moving in a field E = 26 kV/m show that there is not motion of the microtubule perpendicular to its axis. The steering mechanism is thus due to the bending of the leading tip of the microtubule (inset). The change in orientation of the leading end of the microtubule (due to the force component perpendicular to the tip $f_\perp$), determines the trajectory curvature dθ/ds at any point s along the trajectory. Adapted from reference [120] and reproduced with permission.

Using fluorescence microscopy, we image trajectories of a large number of microtubules entering an electric field of magnitude E = 26 kV/m (i.e. under a field-induced perpendicular force $f_\perp$ = 3.2 ± 0.4 pN/µm for microtubules that have a 90° orientation with respect to the electric field (Equation 1.11)). We determine tangent trajectory angles θ and trajectory curvatures dθ/ds for all measured trajectories at every coordinate. Thus, we obtain a large number of orientation-invariant curvatures dθ/ds(sinθ)$^{-1}$, the distribution of which we show Figure 1.14(a). We take the centre of this distribution as

a measure of the mean-orientation invariant curvature at this particular force. We repeated these measurements for a range of electric fields between 0 and 44 kV/m. As expected (Equation 1.10), the mean orientation-invariant curvature increases linearly with E (Figure 1.14(b)). The red line is a linear fit through the data, and from the slope we determine that $\langle d \rangle^2/p = (1.30 \pm 0.16)10^{-10}$ m (Equations 1.10 and 1.11).

Finally, we obtain an estimate for the average tip length $\langle d \rangle$ from observations of the trajectories of very short microtubules that move without any applied electric field. Long microtubules are bound to and propelled by several kinesin molecules distributed along their length and will therefore preserve their directionality. However, if the microtubule length becomes small and comparable to $\langle d \rangle$, then occasionally the filament will be bound to only a single kinesin molecule and display diffusive rotational motion around the motor, thereby rapidly changing its orientation.[123,124] There is a clear relation between the average distance travelled by the microtubule between successive rotations and the ratio of the microtubule length L and the average tip length $\langle d \rangle$[124] Thus, a measurement of $\langle S \rangle$ for a microtubule of known length L provides a measurement of the average tip length $\langle d \rangle$. Using this method, we have measured that in our experiments the average tip length $\langle d \rangle = 0.10 \pm 0.02$ µm.[120]

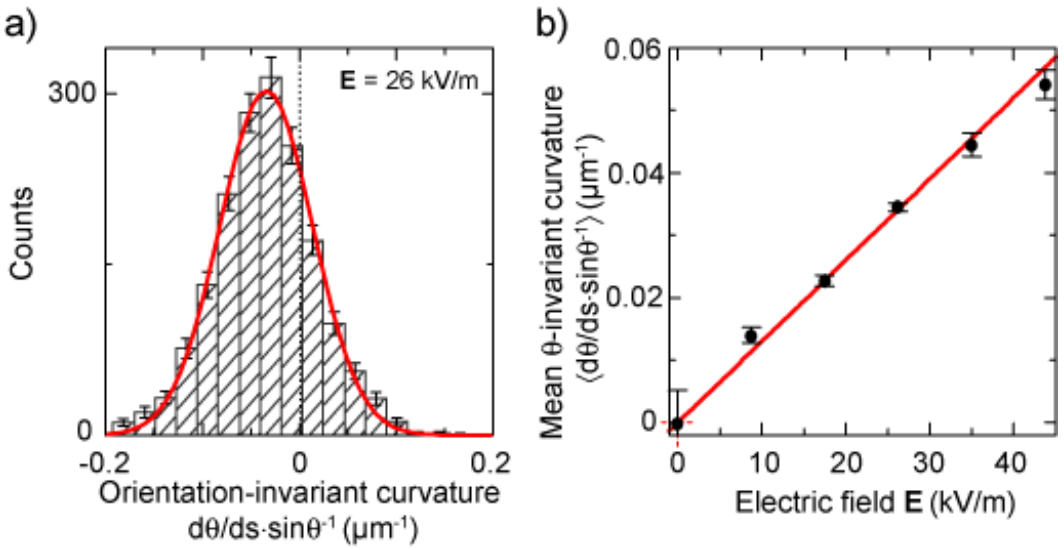

Figure 1.14 Quantification of the trajectory curvatures (a) Distribution of orientation-invariant trajectory curvatures measured from a large number of microtubules under an electric field of E = 26 kV/m. Red line is a Gaussian fit to the data. (b) Mean orientation-invariant curvature (taken as the centre of the distribution in panel a) varies linearly with the electric field, as expected from Equations 1.9 and 1.10. Adapted from reference [120] and reproduced with permission.

With this measurement of $\langle d \rangle$ we determine the persistence length of the leading microtubule ends as $p = 0.08 \pm 0.02$ mm. This value is much smaller than the persistence length of 4-8 mm that is measured for long microtubules.[125,126] Recent experiments have demonstrated that the persistence length of microtubules decreases from 5 mm to 0.11 mm upon decreasing the microtubule contour length from 48 µm down to 2.6 µm.[119] These observations were attributed to the anisotropic mechanical properties of microtubules, which are tubular structures consisting of 13 protofilaments arranged in parallel. In the proposed picture, sliding motion of neighbouring protofilaments induce a compliance in addition to the longitudinal stretching deformations of individual protofilaments. This

leads to the expected decrease of the measured persistence length upon decreasing the deformation length.

An open question remained what happens for shorter lengths L of microtubules that could not be probed in the experiments in reference [119], because the observed $\propto L^{-2}$ decrease in persistence length predicts a vanishingly small persistence length on the $L \approx 0.1$ μm length scale that we probe in our experiments. In contrast, a recently proposed theoretical model, describing the bending of microtubules in terms of bundles of worm-like chains,[127] predicts a saturation of the persistence length upon a further decrease of the deformation length. Our method contributes a measurement of the persistence length of ~0.1 μm long tips, which is one order-of-magnitude smaller than the 2.6 μm length that was previously probed. Nevertheless, the value of $p = 0.08 \pm 0.02$ mm that we find is similar to the 0.11 mm that was measured for the 2.6 μm long microtubules. Moreover, in separate control experiments we established a tip persistence length of 0.24 ± 0.03 mm.[128] Thus our data indicate a lower bound on the persistence length of short lengths of microtubules which is consistent with a recently proposed theory describing the mechanics of wormlike bundles.

In conclusion, we have shown that electric forces in nanofabricated structures are an excellent tool for the study of the mechanical properties of individual biomolecules. We have measured the stiffness of short microtubule ends, which contributes to a better understanding of the mechanical properties of these macromolecules on short length scales.

1.4.3 Electrophoresis of Individual Microtubules in Microfluidic Channels

Finally, we describe the use of micron-size fluidic channels to confine and measure the electrophoresis of freely suspended individual microtubules.[122] Initially, these experiments were performed to measure the mobility of microtubules needed to calibrate the electric field-induced forces in steering experiments mentioned in the previous section. In addition, the high stiffness of microtubules makes them an excellent model system for rod-like particles, which provides an opportunity to measure and test the predicted anisotropy in the electrophoretic mobility for rod-like particles.[129] These experiments also allow us to measure the electrical properties of microtubules, such as the effective charge per tubulin dimer.

We observe the electrophoretic motion of fluorescently labelled microtubules inside 50 x 1 μm^2 slit-like channels that are fabricated between the entrance reservoirs that are separated by 5 mm. The experimental geometry is shown in Figure 1.11(c), with however one important difference: the omission of the kinesin molecules. Upon application of a voltage difference between the electrodes at either end of the channel, we observe that the freely suspended microtubules move in the direction opposite to the electric field. Note that the motion of the negatively charged microtubules in our channels is a superposition of their electrophoretic velocity and any fluid velocity inside the channel due to electro-osmotic flow.

In Figure 1.15(a) we show representative time-lapse images of two microtubules that are driven by an electric field $E = 4$ kV/m. The displacements of these microtubules, which are oriented with their axes approximately equal but in opposite directions to the field, are not collinear with the electric field. Instead, the velocity is slightly directed toward the axis of each microtubule. This orientation-dependent velocity is a hallmark of the anisotropic mobility of a cylindrical particle, Figure 1.15(b). The mobility μ of a microtubule is different for the electric field components perpendicular ($\mu_\perp$, $E_\perp$) and

parallel ($\mu_{//}$, $E_{//}$) to its long axis. Consequently, a microtubule oriented under an angle θ with E (as defined in Figure 1.15(b)), will have velocity components parallel (v_y) and perpendicular (v_x) to the electric field:

$$\begin{aligned} v_x &= \frac{1}{2}(\mu_{//} - \mu_{\perp})\sin(2\theta)E \\ v_y &= \left[(\mu_{//} - \mu_{\perp})\sin^2(\theta) + (\mu_{\perp} + \mu_{EOF})\right]E \end{aligned} \tag{1.12}$$

where μ_{EOF} is the mobility of the electro-osmotic flow in our channels. We determine orientation-dependent velocity for a large number of microtubules. In Figure 1.15(c,d) we show binned values of measured v_x and v_y for microtubules at E = 4 kV/m. As expected from Equation 1.12, microtubules that are oriented under an angle with E move perpendicular to E in the positive x-direction if $\theta < 90^\circ$ and in the negative x-direction otherwise (Figure 1.15(c)). Moreover, microtubules that are oriented parallel to E ($\theta = 90^\circ$) move faster than microtubules that are oriented perpendicular to E ($\theta = 0^\circ$) (Figure 1.15(d)), which is expected if $\mu_{//} \geq \mu_{\perp}$ (Equation 1.12 and References 122 and 129). The red lines in Figure 1.15(c,d) are fits of Equation 1.12 to the data. The fitted amplitude A = $(\mu_{//} - \mu_{\perp})E$ and offset B = $(\mu_{\perp} + \mu_{\mathrm{EOF}})E$ yield information about the different mobility components.

We measured orientation-dependent velocities for different electric fields and display the fitted A and B as a function of E in the insets of Figure 1.15(c,d). From the linear fit through the data we derive the values $(\mu_{//} - \mu_{\perp})$ = -(4.42 ± 0.12) 10^{-9} m^2/Vs, and $(\mu_{\perp} + \mu_{\mathrm{EOF}})$ = -(8.75 ± 0.04)10^{-9} m^2/Vs. In order to determine the values of $\mu_{//}$ and $\mu_{\perp}$, we need to measure the value of the electro-osmotic flow mobility. We do this by a current-monitoring method[122,130] and we find μ_{EOF} = (1.28 ± 0.01)10^{-8} m^2/Vs. This allows us to calculate $\mu_{//}$ = -(2.59 ± 0.02)10^{-8} m^2/Vs and $\mu_{\perp}$ = -(2.15 ± 0.01)10^{-8} m^2/Vs.

The measured mobility anisotropy $\mu_{\perp}/\mu_{//}$ = 0.83 ± 0.01 is clearly different from the well-known factor 0.5 in Stokes-drag coefficients for long cylinders. The reason is that in purely hydrodynamic motion, in which a particle is driven by an external force, the fluid disturbance around a particle is long-range, decaying inversely proportional to the characteristic length scale of the particle. However, in electrophoresis the external electric force acts on the charged particle itself, but as well on the counter ions around the particle. As a result the fluid disturbance around the particle is much shorter range and decays inversely to the cube of the characteristic length scale of the particle.[122,131]

The force on the counterions has important implications for the interpretation of electrophoresis experiments in terms of the effective charge. In previous reports of the electrophoretic mobility of microtubules, their motion was interpreted as a balance between the electric force on the particle and the hydrodynamic Stokes-drag coefficient.[117,132] However, because in hydrodynamic motion the fluid is sheared over a much larger distance than in electrophoresis, this interpretation seriously underestimates the restraining force, which leads to a similarly large underestimation of the effective charge.

Instead, we determine the effective charge of a microtubule by calculation of the ζ-potential and using the Grahame-equation that relates the ζ-potential to effective surface-charge density. For cylinders, the mobility $\mu_{//}$ is directly proportional to the ζ-potential via $\mu_{//} = \varepsilon\zeta\eta$,[129] where ε and η are the solution's dielectric constant and viscosity, respectively. This yields ζ = -32.6 ± 0.3 mV, which corresponds to an effective surface-charge density of -36.7 ± 0.4 mC/m^2. Using the surface area of a microtubule, we calculate an effective

charge of -23 ± 0.2 *e* per dimer.[122] The latter value should be compared to the theoretical bare charge of -47 *e* per dimer, where we attribute the difference to screening due to immobile counter charges that are adsorbed to the microtubule between its surface and the no-slip plane. In contrast, previous reports that ignored the effect of counterions and thereby underestimated the restraining force[117,132] found a bare charge that was up to 5 orders of magnitude lower.

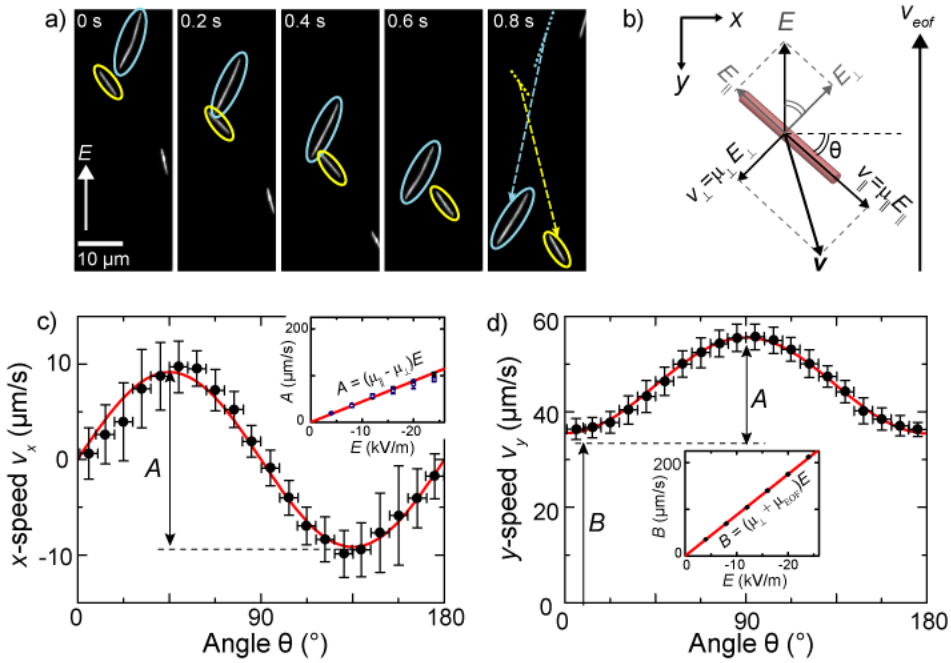

Figure 1.15 Electrophoresis of individual microtubules in microchannels. (a) Electrophoresis of microtubules under an angle with the electric field (E = 4 kV/m) is not collinear with the electric field. (b) A cylinder oriented under an angle θ with E and an anisotropic mobility for electrophoresis perpendicular ($\mu_\perp$) and parallel ($\mu_{//}$) to its axis will have a velocity v that is not collinear with E. The velocity will thus have components parallel (v_y) and perpendicular (v_x) to E (Eq. 1.12). (c) Measured v_x as a function of θ for microtubules at E = 4 kV/m. The solid line is a fit of Eq. 1.11. The inset shows the fitted amplitude A as a function of E. (d) Measured v_y as a function of θ for microtubules at E = 4 kV/m. The solid line is a fit of Equation 1.12. The inset shows the fitted amplitude offset B as a function of E. Adapted from reference [122] and reproduced with permission.

In summary, we have shown that microfabricated channels are an excellent system to measure the electrophoresis of individual microtubules. From these experiments we have gained valuable insights in the fundamental electrophoretic properties of colloidal cylinders and we obtained measurements of the effective surface charge of microtubules.

1.5 ACKNOWLEDGEMENTS

During the various projects we have benefited from the involvement and discussions with K. Besteman, D.J. Bonthuis, C.T. Butcher, Z. Deurvorst, R. Driessen, I. Dujovne, M.P. de Graaff, F.J.H. van der Heyden, W.J.A. Koopmans, M. Kruithof, S.G. Lemay, C. Meyer, Y. Shen, R.M.M. Smeets and with collaborators S. Diez, M. Dogterom, and J. Howard.

References

1. P. S. Dittrich, K. Tachikawa and A. Manz, *Anal Chem*, 2006, **78**, 3887-3907.
2. R. P. Feynman and J. Robbins, *The pleasure of finding things out: the best short works of Richard P. Feynman*, Perseus Books, Cambridge, Mass., 1999.
3. W. D. Volkmuth and R. H. Austin, *Nature*, 1992, **358**, 600-602.
4. S. W. Turner, A. M. Perez, A. Lopez and H. G. Craighead, *Journal of Vacuum Science & Technology B*, 1998, **16**, 3835-3840.
5. J. Han, S. W. Turner and H. G. Craighead, *Phys Rev Lett*, 1999, **83**, 1688-1691.
6. B. Hille, *Ion channels of excitable membranes*, 3rd edn., Sinauer, Sunderland, Mass., 2001.
7. T. E. Springer, T. A. Zawodzinski and S. Gottesfeld, *J Electrochem Soc*, 1991, **138**, 2334-2342.
8. J. Li, D. Stein, C. McMullan, D. Branton, M. J. Aziz and J. A. Golovchenko, *Nature*, 2001, **412**, 166-169.
9. C. Dekker, *Nature Nanotechnology*, 2007, **2**, 209-215.
10. H. A. Stone, A. D. Stroock and A. Ajdari, *Annual Review of Fluid Mechanics*, 2004, **36**, 381-411.
11. T. M. Squires and S. R. Quake, *Rev Mod Phys*, 2005, **77**, 977-1026.
12. H. Y. Wang, R. S. Foote, S. C. Jacobson, J. H. Schneibel and J. M. Ramsey, *Sensors and Actuators B-Chemical*, 1997, **45**, 199-207.
13. S. C. Jacobson, A. W. Moore and J. M. Ramsey, *Anal Chem*, 1995, **67**, 2059-2063.
14. F. H. J. van der Heyden, D. Stein and C. Dekker, *Phys Rev Lett*, 2005, **95**, 116104.
15. D. Stein, F. H. J. van der Heyden, W. J. A. Koopmans and C. Dekker, *Proceedings of the National Academy of Sciences of the United States of America*, 2006, **103**, 15853-15858.
16. F. H. J. van der Heyden, D. J. Bonthuis, D. Stein, C. Meyer and C. Dekker, *Nano Letters*, 2006, **6**, 2232-2237.
17. D. Stein, M. Kruithof and C. Dekker, *Phys Rev Lett*, 2004, **93**, -.
18. J. Lyklema, H. P. v. Leeuwen, M. v. Vliet and A. M. Cazabat, *Fundamentals of interface and colloid science*, Academic Press, London ; San Diego, 1991.
19. S. H. Behrens and M. Borkovec, *Phys Rev E*, 1999, **60**, 7040-7048.
20. A. Ajdari, *Phys Rev E*, 1996, **53**, 4996-5005.
21. S. e. a. Levine, *Faraday Transactions*, 1974, **2**, 1.
22. R. K. Iler, *The chemistry of silica : solubility, polymerization, colloid and surface properties, and biochemistry*, Wiley, New York, 1979.
23. H. Chang, F. Kosari, G. Andreadakis, M. A. Alam, G. Vasmatzis and R. Bashir, *Nano Letters*, 2004, **4**, 1551-1556.
24. R. Fan, M. Yue, R. Karnik, A. Majumdar and P. D. Yang, *Phys Rev Lett*, 2005, **95**, 086607.
25. R. M. M. Smeets, U. F. Keyser, D. Krapf, M. Y. Wu, N. H. Dekker and C. Dekker, *Nano Letters*, 2006, **6**, 89-95.
26. R. Karnik, K. Castelino, R. Fan, P. Yang and A. Majumdar, *Nano Letters*, 2005, **5**, 1638-1642.
27. R. B. Schoch and P. Renaud, *Applied Physics Letters*, 2005, **86**, 253111.
28. R. Karnik, R. Fan, M. Yue, D. Y. Li, P. D. Yang and A. Majumdar, *Nano Letters*, 2005, **5**, 943-948.
29. S. H. Behrens and D. G. Grier, *J Chem Phys*, 2001, **115**, 6716-6721.

30. J. N. Israelachvili and G. E. Adams, *Journal of the Chemical Society-Faraday Transactions I*, 1978, **74**, 975.
31. W. A. Ducker, T. J. Senden and R. M. Pashley, *Nature*, 1991, **353**, 239-241.
32. A. Naji and R. R. Netz, *Physical Review Letters*, 2005, **95**, 185703.
33. C. C. Fleck and R. R. Netz, *Physical Review Letters*, 2005, **95**, 128101
34. H. Boroudjerdi and R. R. Netz, *Journal of Physics-Condensed Matter*, 2005, **17**, S1137-S1151.
35. F. H. J. van der Heyden, D. Stein, K. Besteman, S. G. Lemay and C. Dekker, *Phys Rev Lett*, 2006, **96**, 224502.
36. J. Lyklema, *Journal of Physics-Condensed Matter*, 2001, **13**, 5027-5034.
37. L. Joly, C. Ybert, E. Trizac and L. Bocquet, *Phys Rev Lett*, 2004, **93**, 257805.
38. R. Qiao and N. R. Aluru, *Phys Rev Lett*, 2004, **92**, 198301.
39. A. Y. Grosberg, T. T. Nguyen and B. I. Shklovskii, *Reviews of Modern Physics*, 2002, **74**, 329-345.
40. Y. Levin, *Reports on Progress in Physics*, 2002, **65**, 1577-1632.
41. M. Quesada-Perez, E. Gonzalez-Tovar, A. Martin-Molina, M. Lozada-Cassou and R. Hidalgo-Alvarez, *Chemphyschem*, 2003, **4**, 235-248.
42. B. I. Shklovskii, *Phys Rev E*, 1999, **60**, 5802-5811.
43. K. Besteman, M. A. G. Zevenbergen, H. A. Heering and S. G. Lemay, *Phys Rev Lett*, 2004, **93**, 170802.
44. K. Besteman, M. A. G. Zevenbergen and S. G. Lemay, *Phys Rev E*, 2005, **72**, 061501.
45. P. Kekicheff, S. Marcelja, T. J. Senden and V. E. Shubin, *J Chem Phys*, 1993, **99**, 6098-6113.
46. M. Quesada-Perez, A. Martin-Molina, F. Galisteo-Gonzalez and R. Hidalgo-Alvarez, *Mol Phys*, 2002, **100**, 3029-3039.
47. T. Terao and T. Nakayama, *Phys Rev E*, 2001, **6304**, 041401.
48. Q. Wen and J. X. Tang, *J Chem Phys*, 2004, **121**, 12666-12670.
49. P. J. Scales, F. Grieser and T. W. Healy, *Langmuir*, 1990, **6**, 582-589.
50. J. F. Osterle, *ASME, TRANSACTIONS, SERIES E-JOURNAL OF APPLIED MECHANICS*, 1964, **31**, 161-164.
51. J. Yang, F. Z. Lu, L. W. Kostiuk and D. Y. Kwok, *Journal of Micromechanics and Microengineering*, 2003, **13**, 963-970.
52. H. Daiguji, P. D. Yang, A. J. Szeri and A. Majumdar, *Nano Letters*, 2004, **4**, 2315-2321.
53. W. Olthuis, B. Schippers, J. Eijkel and A. van den Berg, *Sensors and Actuators B-Chemical*, 2005, **111**, 385-389.
54. F. H. J. van der Heyden, D. J. Bonthuis, D. Stein, C. Meyer and C. Dekker, *Nano Letters*, 2007, **7**, 1022-1025.
55. E. Brunet and A. Ajdari, *Phys Rev E*, 2004, **69**, 016306.
56. J. Eijkel, *Lab on a Chip*, 2007, **7**, 299-301.
57. S. Pennathur, J. C. T. Eijkel and A. van den Berg, *Lab on a Chip*, 2007, **7**, 1234-1237.
58. Y. Ren and D. Stein, *Nanotechnology*, 2008, **19**, 195707.
59. E. Lauga, M. P. Brenner and H. A. Stone, in *Handbook of Experimental Fluid Dynamics*, eds. C. Tropea, A. Yarin and J. F. Foss, Springer, New York, Editon edn., 2005.
60. M. Majumder, N. Chopra, R. Andrews and B. J. Hinds, *Nature*, 2005, **438**, 44-44.
61. J. K. Holt, H. G. Park, Y. M. Wang, M. Stadermann, A. B. Artyukhin, C. P. Grigoropoulos, A. Noy and O. Bakajin, *Science*, 2006, **312**, 1034-1037.

62. B. Alberts, *Molecular biology of the cell*, 4th edn., Garland Science, New York, 2002.
63. G. W. Slater, P. Mayer and G. Drouin, *Analusis*, 1993, **21**, M25-M28.
64. J. L. Viovy, *Rev Mod Phys*, 2000, **72**, 813-872.
65. J. Han and H. G. Craighead, *Science*, 2000, **288**, 1026-1029.
66. M. Doi and S. F. Edwards, *The theory of polymer dynamics*, Oxford University Press, New York, 1986.
67. E. F. Casassa, *Journal of Polymer Science Part B-Polymer Letters*, 1967, **5**, 773.
68. E. F. Casassa and Y. Tagami, *Macromolecules*, 1969, **2**, 14.
69. E. A. DiMarzio and C. M. Guttman, *Macromolecules*, 1970, **3**, 131-146.
70. G. Taylor, *Proceedings of the Royal Society of London Series a-Mathematical and Physical Sciences*, 1953, **219**, 186-203.
71. H. Brenner, *Physicochem. Hydrodyn.*, 1980, **1**, 91-123.
72. P.-G. De Gennes, *Scaling concepts in polymer physics*, Cornell University Press, Ithica, 1979.
73. D. S. Cannell and F. Rondelez, *Macromolecules*, 1980, **13**, 1599.
74. Y. L. Chen, M. D. Graham, J. J. de Pablo, G. C. Randall, M. Gupta and P. S. Doyle, *Phys Rev E*, 2004, **70**, 060901.
75. J. O. Tegenfeldt, C. Prinz, H. Cao, S. Chou, W. W. Reisner, R. Riehn, Y. M. Wang, E. C. Cox, J. C. Sturm, P. Silberzan and R. H. Austin, *Proceedings of the National Academy of Sciences of the United States of America*, 2004, **101**, 10979-10983.
76. A. Balducci, P. Mao, J. Y. Han and P. S. Doyle, *Macromolecules*, 2006, **39**, 6273-6281.
77. D. Dutta and D. T. Leighton, *Anal Chem*, 2003, **75**, 57-70.
78. Y. C. Wang, A. L. Stevens and J. Y. Han, *Anal Chem*, 2005, **77**, 4293-4299.
79. J. P. Quirino and S. Terabe, *Science*, 1998, **282**, 465-468.
80. D. S. Burgi and R. L. Chien, *Anal Chem*, 1991, **63**, 2042-2047.
81. P. Gebauer, J. L. Beckers and P. Bocek, *Electrophoresis*, 2002, **23**, 1779-1785.
82. J. Astorga-Wells and H. Swerdlow, *Anal Chem*, 2003, **75**, 5207-5212.
83. S. Song, A. K. Singh and B. J. Kirby, *Anal Chem*, 2004, **76**, 4589-4592.
84. J. Khandurina, S. C. Jacobson, L. C. Waters, R. S. Foote and J. M. Ramsey, *Anal Chem*, 1999, **71**, 1815-1819.
85. D. Stein, Z. Deurvorst, F. J. H. v. d. Heyden, W. J. A. Koopmans and C. Dekker, *submitted*, 2008.
86. M. C. Williams, *Proceedings of the National Academy of Sciences of the United States of America*, 2007, **104**, 11125-11126.
87. S. Jun and B. Mulder, *Proceedings of the National Academy of Sciences of the United States of America*, 2006, **103**, 12388-12393.
88. D. J. Bonthuis, C. Meyer, D. Stein and C. Dekker, *submitted*, 2008.
89. J. H. Vanvliet, M. C. Luyten and G. Tenbrinke, *Macromolecules*, 1992, **25**, 3802-3806.
90. T. Odijk, *Polymer*, 1978, **19**, 989-990.
91. T. Odijk, *Macromolecules*, 1983, **16**, 1340-1344.
92. R. P. Feynman, *The pleasure of finding things out*, Penguin books, 1999.
93. J. Howard, *Mechanics of motor proteins and the cytoskeleton*, Sinauer Associates, Inc, Sunderland, Massachusetts, 2001.
94. J. M. Scholey, I. Brust-Mascher and A. Mogilner, *Nature*, 2003, **422**, 746-752.
95. H. C. Berg, *Annual Review Of Biochemistry*, 2003, **72**, 19-54.
96. R. D. Vale, *Cell*, 2003, **112**, 467-480.
97. R. D. Vale and R. A. Milligan, *Science*, 2000, **288**, 88-95.

98. K. Svoboda, C. F. Schmidt, B. J. Schnapp and S. M. Block, *Nature*, 1993, **365**, 721-727.
99. E. Meyhofer and J. Howard, *Proceedings Of The National Academy Of Sciences Of The United States Of America*, 1995, **92**, 574-578.
100. M. J. Schnitzer and S. M. Block, *Nature*, 1997, **388**, 386-390.
101. W. Hua, E. C. Young, M. L. Fleming and J. Gelles, *Nature*, 1997, **388**, 390-393.
102. D. L. Coy, M. Wagenbach and J. Howard, *Journal Of Biological Chemistry*, 1999, **274**, 3667-3671.
103. M. G. L. van den Heuvel and C. Dekker, *Science*, 2007, **317**, 333-336.
104. H. Hess, G. D. Bachand and V. Vogel, *Chemistry-a European Journal*, 2004, **10**, 2110-2116.
105. H. Hess, *Soft Matter*, 2006, **2**, 669-677.
106. R. Mukhopadhyay, *Analytical Chemistry*, 2005, **77**, 249A-252A.
107. S. Ramachandran, K. H. Ernst, G. D. Bachand, V. Vogel and H. Hess, *Small*, 2006, **2**, 330-334.
108. G. D. Bachand, S. B. Rivera, A. Carroll-Portillo, H. Hess and M. Bachand, *Small*, 2006, **2**, 381-385.
109. M. G. L. van den Heuvel, M. P. De Graaff and C. Dekker, *Science*, 2006, **312**, 910-914.
110. C. T. Lin, M. T. Kao, K. Kurabayashi and E. Meyhofer, *Small*, 2006, **2**, 281-287.
111. Y. Hiratsuka, T. Tada, K. Oiwa, T. Kanayama and T. Q. P. Uyeda, *Biophysical Journal*, 2001, **81**, 1555-1561.
112. S. G. Moorjani, L. Jia, T. N. Jackson and W. O. Hancock, *Nano Letters*, 2003, **3**, 633-637.
113. H. Hess, C. M. Matzke, R. K. Doot, J. Clemmens, G. D. Bachand, B. C. Bunker and V. Vogel, *Nano Letters*, 2003, **3**, 1651-1655.
114. M. G. L. van den Heuvel, C. T. Butcher, R. M. M. Smeets, S. Diez and C. Dekker, *Nano Letters*, 2005, **5**, 1117-1122.
115. M. Sundberg, J. P. Rosengren, R. Bunk, J. Lindahl, I. A. Nicholls, S. Tagerud, P. Omling, L. Montelius and A. Mansson, *Analytical Biochemistry*, 2003, **323**, 127-138.
116. D. Riveline, A. Ott, F. Julicher, D. A. Winkelmann, O. Cardoso, J. J. Lacapere, S. Magnusdottir, J. L. Viovy, L. Gorre-Talini and J. Prost, *European Biophysics Journal*, 1998, **27**, 403-408.
117. R. Stracke, K. J. Bohm, L. Wollweber, J. A. Tuszynski and E. Unger, *Biochemical and Biophysical Research Communications*, 2002, **293**, 602-609.
118. M. G. L. Van den Heuvel, C. T. Butcher, S. G. Lemay, S. Diez and C. Dekker, *Nano Letters*, 2005, **5**, 235-241.
119. F. Pampaloni, G. Lattanzi, A. Jonas, T. Surrey, E. Frey and E. L. Florin, *Proceedings Of The National Academy Of Sciences Of The United States Of America*, 2006, **103**, 10248-10253.
120. M. G. L. van den Heuvel, M. P. de Graaff and C. Dekker, *PNAS*, 2008, **in press**.
121. D. Stigter and C. Bustamante, *Biophysical Journal*, 1998, **75**, 1197-1210.
122. M. G. L. van den Heuvel, M. P. de Graaff, S. G. Lemay and C. Dekker, *PNAS*, 2007, **104**, 7770-7775.
123. A. J. Hunt and J. Howard, *Proceedings Of The National Academy Of Sciences Of The United States Of America*, 1993, **90**, 11653-11657.
124. T. Duke, T. E. Holy and S. Leibler, *Physical Review Letters*, 1995, **74**, 330-333.
125. M. E. Janson and M. Dogterom, *Biophysical Journal*, 2004, **87**, 2723-2736.
126. F. Gittes, B. Mickey, J. Nettleton and J. Howard, *Journal Of Cell Biology*, 1993, **120**, 923-934.

127. C. Heussinger, M. Bathe and E. Frey, *Physical Review Letters*, 2007, **99**.
128. M. G. L. van den Heuvel, S. Bolhuis and C. Dekker, *Nano Letters*, 2007, **7**, 3138-3144.
129. D. Stigter, *Journal Of Physical Chemistry*, 1978, **82**, 1417-1423.
130. X. H. Huang, M. J. Gordon and R. N. Zare, *Analytical Chemistry*, 1988, **60**, 1837-1838.
131. D. Long and A. Ajdari, *European Physical Journal E*, 2001, **4**, 29-32.
132. L. L. Jia, S. G. Moorjani, T. N. Jackson and W. O. Hancock, *Biomedical Microdevices*, 2004, **6**, 67-74.

http://www.springer.com/978-0-85404-147-3

Nanofluidics
Nanoscience and Nanotechnology
(Eds.)J.B. Edel; A.J. Mello
2009, Hardcover
ISBN: 978-0-85404-147-3
A product of Royal Society of Chemistry